



HAL
open science

Contributions of an innovative post-weld heat treatment to the micro-tensile behavior of two mono-material linear friction welded joints using: The β -metastable Ti-5Al-2Sn-2Zr-4Mo-4Cr (Ti17) and the near- α Ti-6Al-2Sn-4Zr-2Mo (Ti6242) Ti-alloys
Dorick Ballat-Durand, Salima Bouvier, Marion Risbet

► **To cite this version:**

Dorick Ballat-Durand, Salima Bouvier, Marion Risbet. Contributions of an innovative post-weld heat treatment to the micro-tensile behavior of two mono-material linear friction welded joints using: The β -metastable Ti-5Al-2Sn-2Zr-4Mo-4Cr (Ti17) and the near- α Ti-6Al-2Sn-4Zr-2Mo (Ti6242) Ti-alloys. *Materials Science and Engineering: A*, 2019, 766, pp.138334. 10.1016/j.msea.2019.138334 . hal-02889610

HAL Id: hal-02889610

<https://hal.science/hal-02889610>

Submitted on 20 Jul 2022

HAL is a multi-disciplinary open access archive for the deposit and dissemination of scientific research documents, whether they are published or not. The documents may come from teaching and research institutions in France or abroad, or from public or private research centers.

L'archive ouverte pluridisciplinaire **HAL**, est destinée au dépôt et à la diffusion de documents scientifiques de niveau recherche, publiés ou non, émanant des établissements d'enseignement et de recherche français ou étrangers, des laboratoires publics ou privés.



Distributed under a Creative Commons Attribution - NonCommercial 4.0 International License

Contributions of an innovative post-weld heat treatment to the micro-tensile behavior of two mono-material Linear Friction Welded joints using: the β -metastable Ti-5Al-2Sn-2Zr-4Mo-4Cr (Ti17) and the near- α Ti-6Al-2Sn-4Zr-2Mo (Ti6242) Ti-alloys.

Dorick BALLAT-DURAND¹, Salima BOUVIER¹, Marion RISBET¹

¹Alliance Sorbonne Université, Université de Technologie de Compiègne, Laboratoire Roberval de Mécanique, CNRS FRE 2012, CS 60319 Rue Roger Couitolenc 60203 Compiègne cedex France

Corresponding author: dorick.ballat-durand@utc.fr, Tel. 00 33 3 44 23 40 51,

salima.bouvier@utc.fr, marion.risbet@utc.fr

Abstract

The mechanical behavior of two mono-material Ti-alloy joints obtained by Linear Friction Welding (LFW) were investigated through micro-tensile testing combined with full-field measurements; the resulting tensile behaviors were examined in dependence of the local microstructures and crystallographic features. The near- α Ti-6Al-2Sn-4Zr-2Mo (Ti6242) and the β -metastable Ti-5Al-2Sn-2Zr-4Mo-4Cr (Ti17) welds were tested up to failure in both as-welded (AW) and heat treated (PWHT) configurations. In the AW Ti17 joint, the dissolution of the hardening α precipitates in favor of a $\beta_{\text{metastable}}$ phase resulted in a remarkable loss in stiffness and strength compared to the as-received Widmanstätten $\alpha+\beta$ base material (BM). The gradients of microstructure led to significant heterogeneities in the local mechanical behaviors and subsequent strain incompatibilities between the refined weld center line (WL) and the neighboring coarse-

grained thermo-mechanically affected zone (TMAZ). These features caused an early and intense strain localization in the joint ultimately causing failure by quasi-cleavage at the WL/TMAZ border. Transforming the AW microstructures through β annealing followed by $\alpha+\beta$ ageing permitted to form back a Widmanstätten $\alpha+\beta$ microstructure in the whole assembly resulting in homogenized elastic and plastic behaviors. In the joint core of the AW Ti6242, the precipitation of α'/α'' martensitic laths or $\alpha_{\text{secondary}}$ fragments upon cooling the high temperature $\beta_{\text{transformed}}$ microstructure caused a noteworthy refinement and a consistent weld overmatch; a slight loss of stiffness was also noted. The microstructures neighboring the refined joint did not exhibit singular microstructural changes but the dissolution of $\alpha_{\text{secondary}}$ platelets initially hardening the β matrix and a probable resorption of hardening particles. These phenomena appeared to have weakened these heat-affected zones (HAZ) leading to an intense slip occurrence in the latter and a quasi-cleavage fracture. The heat treatment consisting of an $\alpha+\beta$ annealing followed by ageing permitted to homogenize the stiffness values through the reprecipitation of equilibrium $\alpha+\beta$ microstructures across the joint. The formerly softened HAZ was hardened back and exhibited a mechanical behavior similar to the neighboring BM. A gradual microstructure refinement was preserved across the joint ensuring a remaining slight weld overmatch.

1. Introduction

The interest in using Ti-alloys for structural applications within the aerospace industry has constantly risen for the past three decades. This increase is related to the advantageous specific strength of these alloys associated with favorable thermal and electro-chemical compatibility with Carbon-Fiber Reinforced Plastics (CFRP). Furthermore the objectives of costs and weight reduction led the manufacturers to

increase the number of functions handled by each part as well as to favor welding at the expense of mechanical assemblies. Such a strategy resulted in an escalation in the shape complexity of the structural parts and ultimately in the development of machining pre-shapes to limit the machining costs and to improve the buy-to-fly ratio. Additive manufacturing and welding techniques appeared promising to produce these pre-shapes. However, welding Ti-alloys is known to be challenging using common fusion techniques as solidification defects [1], [2], and embrittling oxygen/nitrogen pollution could occur within the joint if the protective environment is deficient [3], [4]. Thus solid-state joining processes are considered as encouraging alternative techniques for joining Ti-alloys since they are believed to prevent these issues [5], [6].

Linear Friction Welding (LFW) belongs to these so-called solid-state joining processes. Yet, contrary to Friction Stir Welding (FSW), the heat and joining in LFW is solely achieved by the friction between the two work-pieces to be assembled (i.e. no welding tool is involved in the joint): one forging part is pressed against a second work piece describing an oscillating linear motion (oscillating part), the contact friction generates heat and wear which leads ultimately to joining. Four distinct process stages, schematized in *Figure 1*, were identified during LFW by the authors in [6]–[8] as:

- The contact stage 1: The two parts are brought into contact initially resting on surface asperities followed by an increase in the contact area due to asperity flattening.
- The initial stage 2: The large particles are expelled from the interface and the friction on the asperities leads to a local heating; the latter forming hot spots which initiates material joining and the axial shortening.
- The friction stage 3: The heat and joining extends up to the entire contact interface leading to severe local shear deformation and a subsequent heating; the joint is no longer able to handle the axial load which results in an extensive material extrusion.

- The forging stage 4: Once the axial shortening condition is fulfilled, the oscillating motion stops and the weld is consolidated by holding the axial pressure; fast cooling of the joint is ensured by heat diffusion into each work pieces.

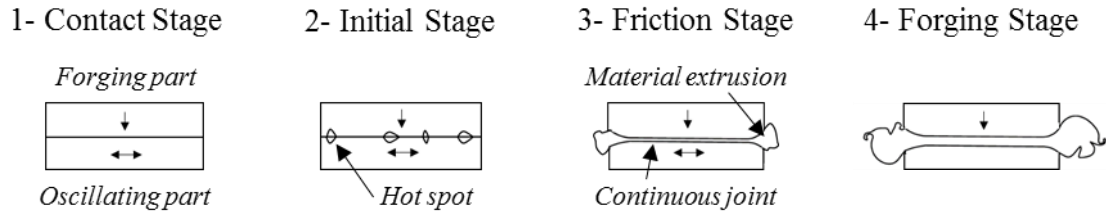


Figure 1 : Schematic representation of the four process stages involved in LFW Ti-alloys

Generally Ti-alloys have been found to be excellent candidates for LFW due to their following properties: 1) a fairly low thermal conductivity that limits the energy dissipation to the bulk resulting in a fast and localized material heating; 2) the $\alpha \rightarrow \beta$ phase transformation happening during the process [8]–[10] that allows strong metal/metal bonds between the body-centered cubic (BCC) β lattices [11]; 3) The propensity of the β phase to accommodate large plastic deformations in the β -domain [12], [13] which enables the use of large amplitudes (2-3 mm) for a consistent heat generation. Numerous studies investigated the weldability, microstructures and the mechanical behavior of the widely used $\alpha+\beta$ Ti64 [7], [14]–[18] and showed that a thin hard joint is formed characterized by a significant microstructure refinement and a subsequent weld overmatch. The monotonic tensile tests and fatigue tests resulted mostly in failure in the parent material (i.e. far from the weld). Yet, the growing interest on alternative Ti-alloys for specific uses (in place of the multi-purpose $\alpha+\beta$ Ti64) has brought few authors into investigating β -metastable [9], [19]–[21] or near- α [10], [22]–[25] LFW joints. These studies showed that the results obtained on the $\alpha+\beta$ Ti64

are not transposable to every Ti-alloys as: the as-welded microstructures are highly related to the intrinsic properties of each alloys as well as to the initial microstructures. Thus, subjecting the as-welded microstructures to improper Post-Weld Heat Treatments (PWHT) resulted in undesirable effects: an embrittlement of the $\beta\beta$ -metastable joints [26], [27] and a drop in toughness of the near- α joints [23].

Preceding studies performed by the authors were focused on mono-material assemblies of the β -metastable Ti17 and the near- α Ti6242 in [9], [10] respectively. These papers were endeavored to advanced microstructural characterizations, and to the identification of the transformation mechanisms involved during the process. The following major findings were drawn: 1) remarkable gradients of thermo-mechanical loads were present within the welds during the process, this resulted in deep microstructure changes through phase transformations and the activation of recrystallization/recovery mechanisms; 2) the joints were characterized by significant microstructure heterogeneities, local metastable states (martensitic α' or mechanically unstable β_m), and consistent discontinuous hardness properties. These particular microstructures and mechanical properties drove the authors to develop a specific heat treatment which permitted to reduce/resorb the microstructure gradients as well as obtaining stable hardness properties across the assemblies. This PWHT consisted of an annealing at 910 °C for 2 h followed by furnace cooling to 635 °C in 2 h, then ageing was performed at 635 °C for 8 h followed by air cooling. However, hardness tests could not provide enough information to identify the local mechanical viability of the as-welded joints and the contributions of a PWHT to it.

In this paper, the authors aimed at identifying the relationship between the mechanical properties and the local microstructures, before and after this PWHT, across two mono-material LFW joints using: the β -metastable Ti-5Al-2Sn-2Zr-4Mo-4Cr

(Ti17) and the near- α Ti-6Al-2Sn-4Zr-2Mo (Ti6242) Ti-alloys. A detailed analysis combining full-field measurements and microstructural investigations will be proposed to characterize in depth the mechanisms affecting the local responses to monotonic tensile tests. Such a study will demonstrate the beneficial effects of this PWHT on the macroscopic mechanical behaviors compared to the metastable AW configurations. Information on the joints durability to high cycle fatigue tests can be found elsewhere in [28] and [29] for the Ti6242 and the Ti17 respectively.

2. Material and methods

The joints were obtained using a MDS-30 within the facilities of the company ACB, Nantes, France. The assemblies were welded with the following LFW process parameters: a forging pressure of 90 MPa, an amplitude of 2 mm, a frequency of 50 Hz, and an axial shortening of 3 mm. The assemblies consisted of two blocks of 15*80*70 mm³ of similar materials butt welded with: the 15*80 mm² surface as the initial contact surface, the 80 mm edge as the oscillating direction, and the 70 mm edge as the forging direction (*Figure 2*). Each blocks were obtained by electrical discharge machining (EDM) from forged billets of TIMETAL®6-2-4-2 and TIMETAL®17. The complete chemical compositions of each alloys are detailed in *Table 1*; the parent materials were received in the solution treated then aged configuration (STA) from TIMET Savoie S.A., France. The PWHTs were performed on the whole assemblies using a Nabertherm P330 oven under an Argon protective atmosphere.

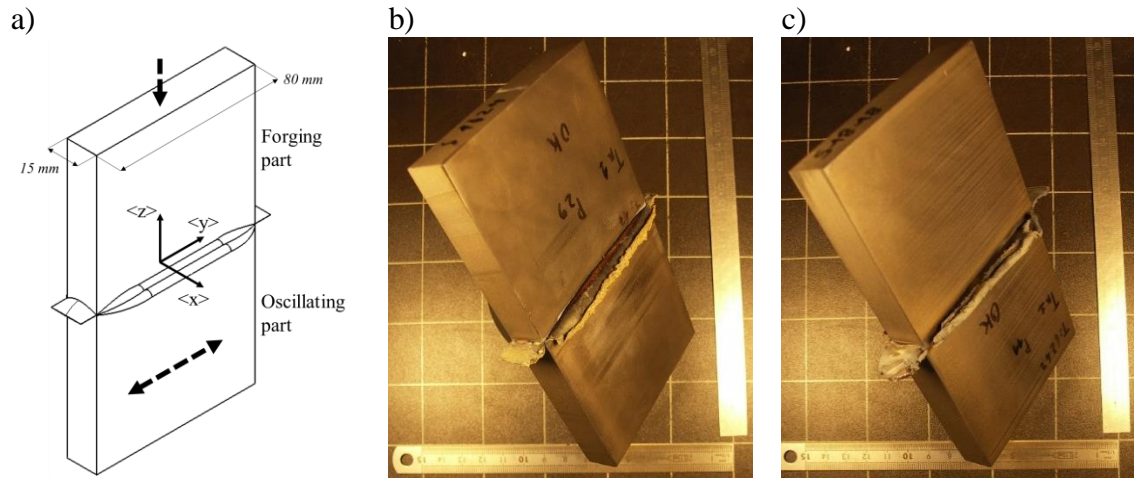


Figure 2 : a) sketch of the assembly detailing the dimensions of the welded parts and the main process directions; pictures of the whole Ti17 and Ti6242 joints in b) and c) respectively.

Table 1 : Chemical compositions in mass (Ti being the balance) and the tensile properties provided by the manufacturer for the two investigated Ti-alloys; E is the Young's modulus, $\sigma_{0.2\%}$ is the yield strength at 0.2% offset, UTS is the ultimate tensile strength, and A% the elongation at break.

Alloy	Alloying elements (w%)							Tensile properties			
	Al	Sn	Zr	Mo	Cr	Si	Ti	E (GPa)	$\sigma_{0.2\%}$ (MPa)	UTS (MPa)	A%
Ti17	5	2	2	4	4	N/A	Bal.	110	1019	1110	15%
Ti6242	6	2	4	2	N/A	0.1	Bal.	115	895	1000	12%

The tensile test specimens were cut to the dimensions detailed in Figure 3 by pre-cutting 1 mm plates using a cut-off machine followed by water jet machining at Microjet, Herrlisheim, France. The samples tested for each LFW configurations were cut at the very center of the assemblies, one of their {xz} surface was polished and

etched to precisely identify the position of the weld and the crack path. The microstructure observations were performed using specific samples on the {yz} surface; both {xz} and {yz} cuts exhibit analogous microstructure changes. The surface preparation consisted of: 1) coarse polishing using grid papers at 100 rpm, P80, P220, P1200, P2400 and P4000; 2) semi-finishing using polyester cloth polishing, first with a 6 μm diamond suspension then with a Struers oxide polish suspension (OPS) for 2 min each at 100 rpm; 3) finishing using vibratory polishing with a solution composed by 50 ml of OPS and 50 ml of H_2O on a Buehler VibroMet 2 for 24 h under a load of 200 g; 4) etching using 2 ml HF, 98 ml H_2O [30] for 12s for the Ti6242 and 30 ml HNO_3 , 3 ml HF and 67 ml H_2O [30] for 3 min for the Ti17. Optical Microscopy (OM) observations were performed on an Olympus BX41M to precisely identify the position of the weld center line for each specimen. Micro-scale observations were performed on a Zeiss Sigma Scanning Electron Microscope (SEM). The Matlab[©] tool box Mtex 5.1.1 was used for crystallography-related analysis using the subroutines detailed in [31].

The monotonic micro-tensile tests were performed using a Kammrath & Weiss micro tensile test machine (10 kN) driven through displacement at 12 $\mu\text{m/s}$ up to failure at the Ecole Centrale de Lille, France. The micro-machine was synchronized with a Ximea XiC camera recording changes in the positions of a black and white speckle on the {xz} surface of the specimen (one frame per second). This speckle was obtained by airbrushing fine droplets on a black background layer. The local displacement fields during the tests were determined through Digital Image Correlation (DIC) from the black and white speckle. The DIC was performed using open access Matlab[©] codes available at Digital Image Correlation and Tracking [32]; a step size of 20 pixels ($\approx 68 \mu\text{m}$) and a median filter to the first neighbors were used (*Figure 4*). The local displacements were acquired over a region of interest of approximately 10*2 mm^2 .

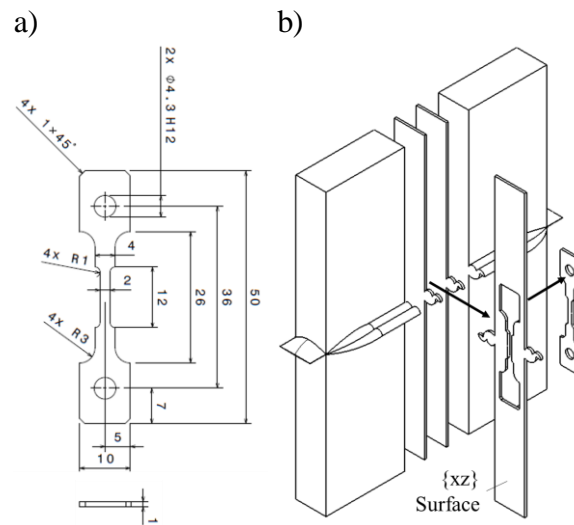


Figure 3 : a) Dimensions in [mm] of the specimens dedicated to micro-tensile testing;
 b) sampling methods of the plates within the joint.

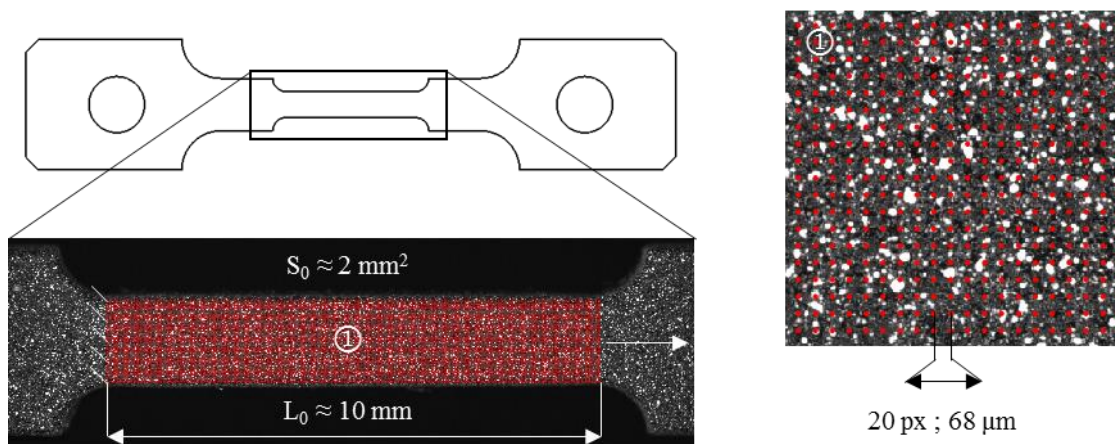


Figure 4 : Position of the region of interest (ROI) on the micro-tensile test samples detailing the gauge length L_0 and the cross-section S_0 ; the integration points for the DIC are shown as red dots within the white speckle.

A specific space-time approach will be used in this study to highlight the inhomogeneous deformation behaviors within the assemblies. The full-field

measurements will be presented as spatio-temporal graphs [28], [33] depicting the evolution of the mean elongation profile across the weld while loading. The three stages to obtain such spatio-temporal graphs are schematized in *Figure 5* as: 1) the local elongations within the ROI are obtained for each DIC frame; 2) the corresponding average elongation profiles are calculated for the three applied strains ($\epsilon_1 < \epsilon_2 \ll \epsilon_3$); 3) each profile is normalized by its maximum value and plotted as an intensity map in dependence on the $\langle z \rangle$ position and the applied macroscopic strain.

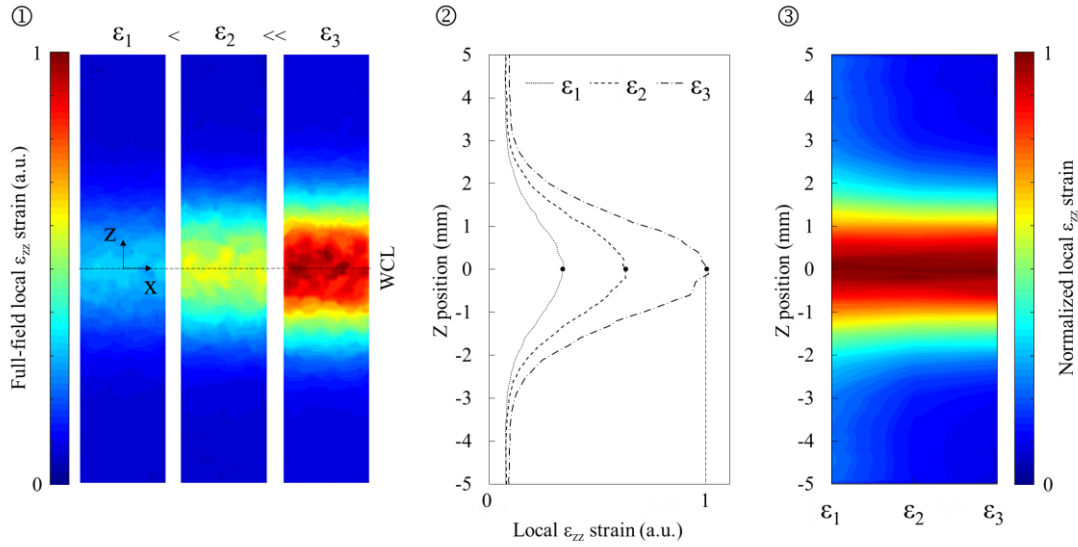


Figure 5 : Schematic representation of the spatio-temporal graphs (marker ③) depicting the average ϵ_{zz} strain profiles (marker ②) obtained for each full-field measurement data sets (marker ①) as an normalized intensity map in dependence on the position to the weld center line (WCL ; $z = 0$) and the applied macroscopic strain (ϵ_1 ; ϵ_2 ; ϵ_3).

Local numerical gauges will be used in this study to investigate and compare the mechanical behaviors of the macro-zones constituting the tested joints before and after

the PWHT. The data obtained from the full-field measurements and the force sensor will be used to determine the local engineering and true stress/strain curves (restricted by the macroscopic necking onset). Several indicators of the mechanical behavior will be extracted from the latter such as: the stiffness, the yield strength, and the work hardening exponent (ranging from the yield point at 0.5% offset to the onset of necking $\sigma_{necking}$). A schematic representation of this protocol is shown in *Figure 6*. However, since the microstructures are heterogeneous and that the micro-tensile samples do not fulfill the representative elementary volume (REV) conditions, the subsequent provided data will solely be considered for comparison purposes.

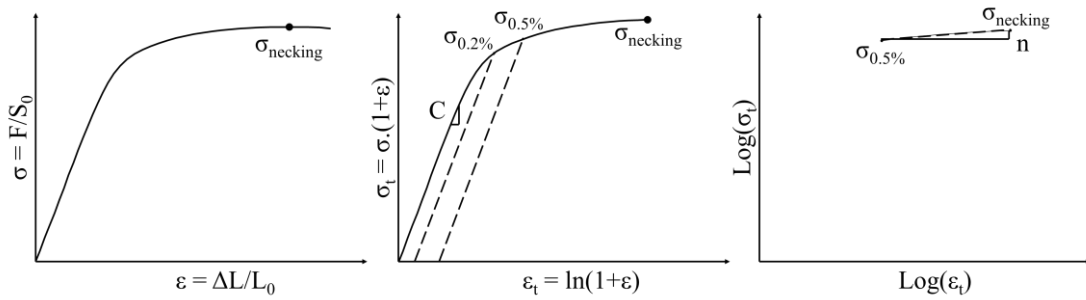


Figure 6 : Schematic representation of the protocol used for determining the stiffness C , yield strength $\sigma_{0.2\%}$ and work hardening exponent n (ranging from the yield point at 0.5% offset to the onset of necking) of the joint macro-zones from the local true stress/strain curve (middle) estimated from the parent engineering one (left).

3. Results and discussions

3.1. Ti17 LFW joint

3.1.1. Microstructure

Preceding work performed by the authors aimed at characterizing the microstructural changes resulting from LFW the β -metastable Ti17 with a Widmanstätten $\alpha+\beta$ starting microstructure [9]. The microstructures and hardness properties of the joint before and after the PWHT are displayed in *Figure 7*.

The gradients of thermo-mechanical loads experienced by the material during the process resulted in significant microstructural changes affecting the crystallographic phases and/or the grain morphologies; both having remarkable effects on the local mechanical properties. Three distinct macro-zones can be identified from these changes: the Welding Line (WL ; $|z| \leq 200 \mu\text{m}$) made of recrystallized highly textured β subgrains ($\langle 110 \rangle$ direction almost aligned with $\langle x \rangle$ and the $\langle 111 \rangle$ direction aligned with the oscillation direction $\langle y \rangle$); the Thermo-Mechanically Affected Zone (TMAZ ; $200 \leq |z| \leq 1200 \mu\text{m}$) consisting of deformed large β grains with traces of transformed “Ghost” α morphologies; and the Heat Affected Zone (HAZ ; $1200 \leq |z| \leq 2600 \mu\text{m}$) indistinguishable from the base material (BM) by imaging techniques but displaying a loss of hardness due to a partial $\alpha \rightarrow \beta$ transformation. The Process Affected Zone (PAZ ; $|z| \leq 2600 \mu\text{m}$) includes all the macro-zones depicted previously.

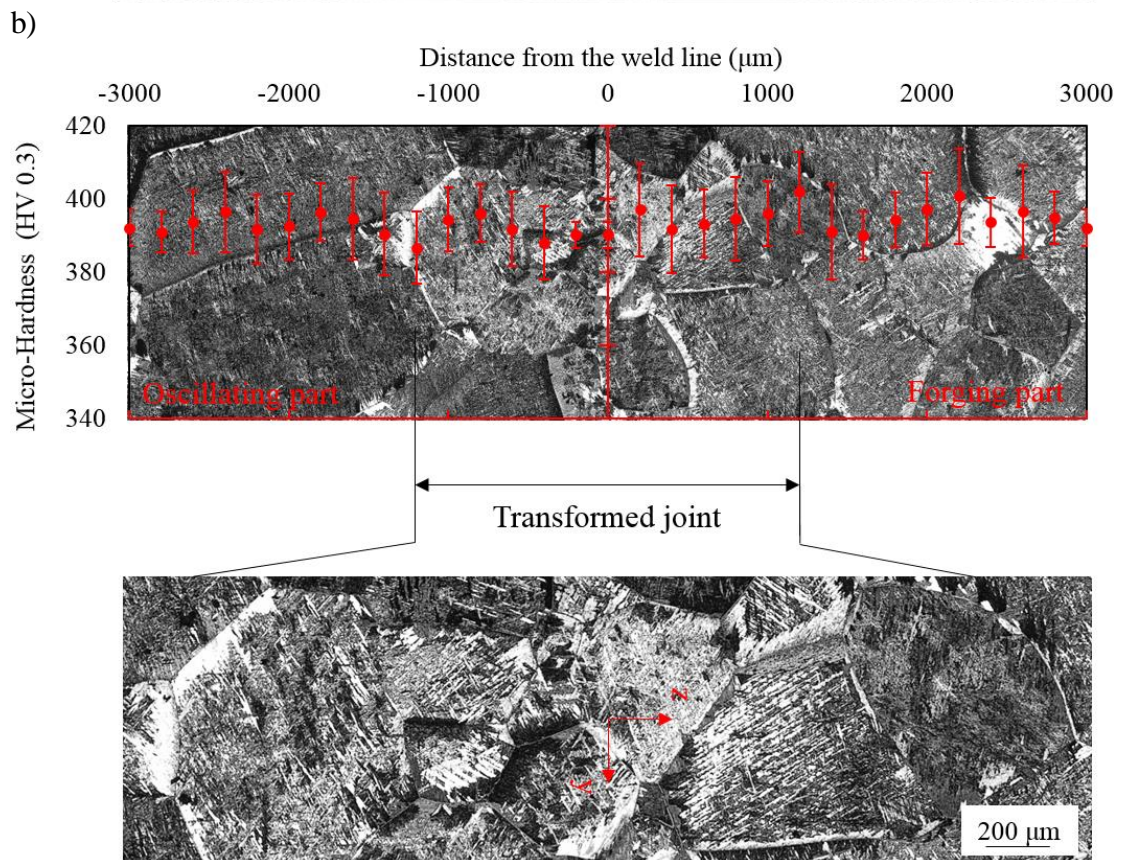
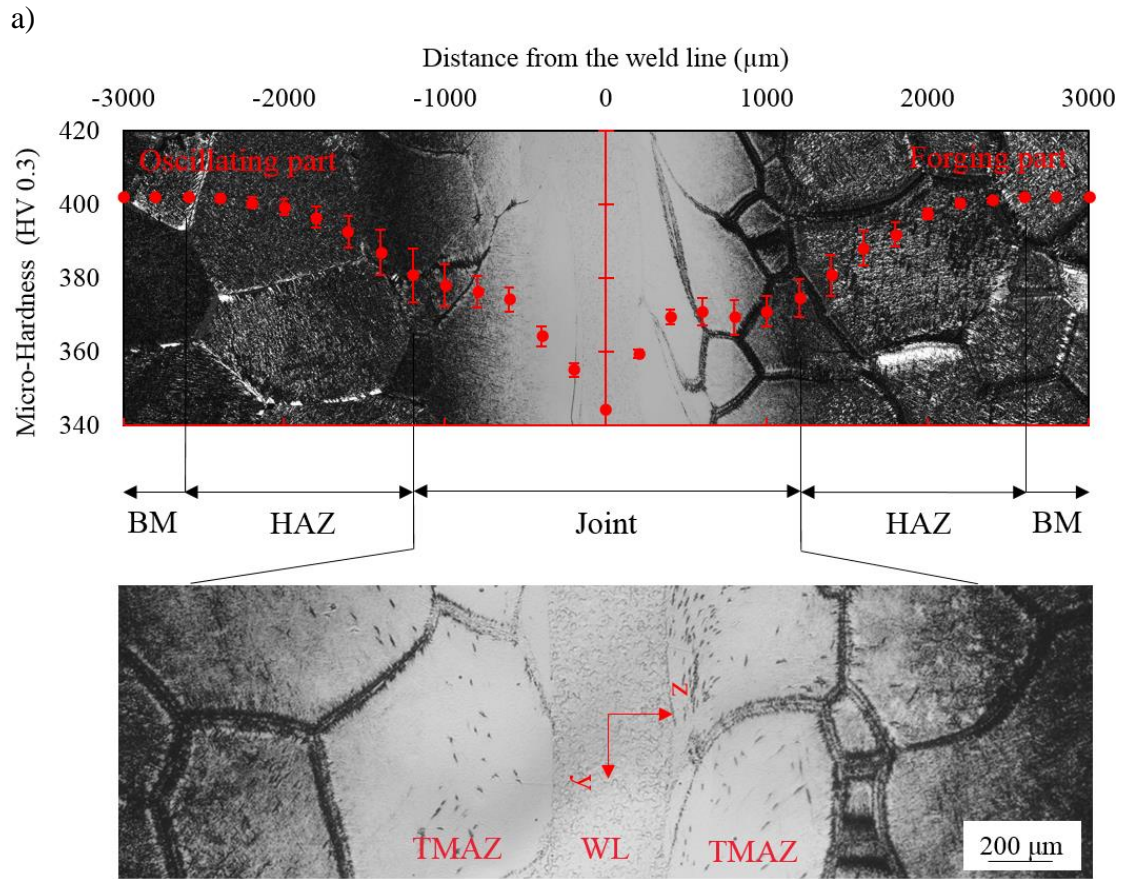


Figure 7 : Combined data from OM bright-field observations and the corresponding local hardness across the Ti17 LFW joint in a) the as-welded (AW) configuration and b) after a Post-Weld Heat Treatment (PWHT); z_0 is set at the weld center line.

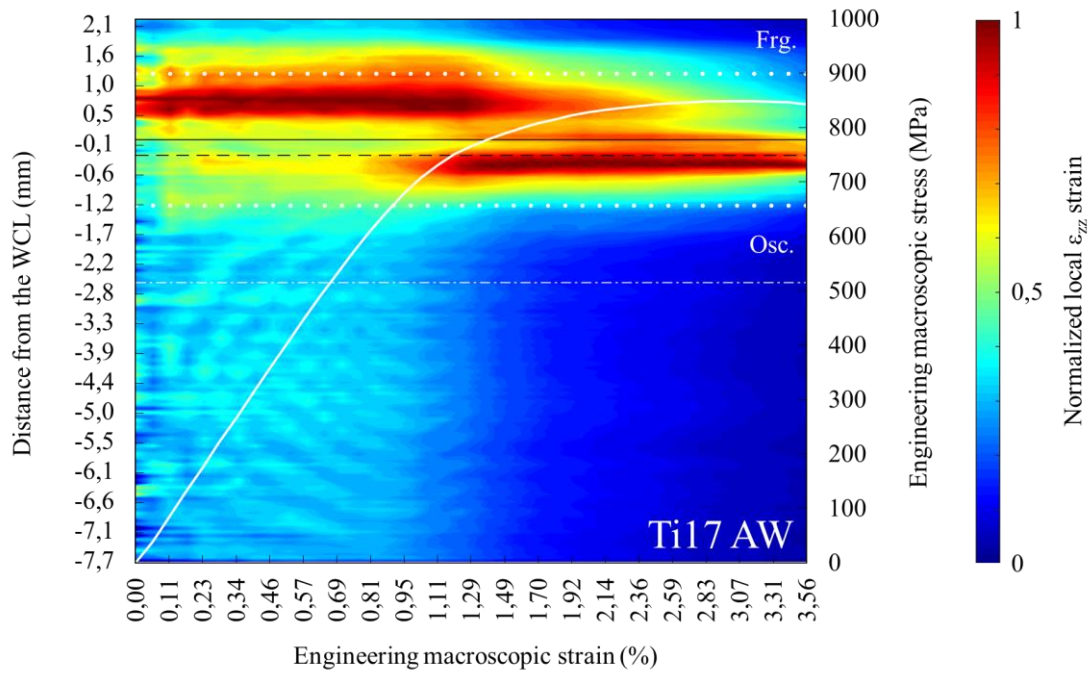
These microstructural changes led to a gradual decrease in hardness from the base material to the TMAZ due to the dissolution of the hardening α precipitates, and from the TMAZ to the WL through dislocation arrangement into subgrains. Furthermore the partial or complete $\alpha+\beta\rightarrow(\alpha)+\beta_{\text{transformed}}$ transformation led to retaining a $\beta_{\text{metastable}}$ (β_m) phase upon cooling in place of the high temperature β_t . Such Ti17 (α)+ β_m microstructures could be prone to a stress-induced martensitic (SIM) transformation that precipitates orthorhombic α'' laths within BCC β_m parent grains [34], [35]. The triggering stress for this SIM transformation depends on the local chemical compositions, the parent β grain size and the dislocation density [36]. Furthermore this transformation and pure elastic deformation of the β_m phase could occur simultaneously thus affecting the apparent stiffness of the sample [37], [38]. The PWHT transformed the local (α)+ β_m microstructure in favor of a Widmanstätten $\alpha+\beta$ mixture ensuring microstructural features (i.e. phase ratio, prior- β grain diameter, α lath size and hardness properties) similar to the ones of the as-received base material. Yet the prior- β grains in the former WL remained two times smaller ($D=500\ \mu\text{m}$) than the ones in the rest of the material ($D=1\ \text{mm}$) and traces of the initial $\{110\}\langle 111\rangle$ texture of the β phase were still measurable after grain growth.

3.1.2. Micro-tensile test response

Monotonic micro-tensile tests were conducted up to failure on each configurations: the as-welded (AW) and the heat treated (PWHT). The PAZ and the WL+TMAZs constitute respectively 50% and 25% of the total gauge length L_0 ($L_0 \approx 10$ mm). The tests outcomes are plotted in *Figure 8* in the form of: 1) macroscopic engineering stress/strain curves (solid white); 2) intensity maps of the spatio-temporal graphs depicting the local ε_{zz} strain in dependence on the $\langle z \rangle$ position and the applied macroscopic longitudinal strain (see section 4.2), each profiles are normalized by their maximum value to emphasize potential heterogeneous behaviors and strain localizations. The approximate $\langle z \rangle$ positions of the WL (black solid line) and the final crack paths (black dashed line) are also provided along with the limits of the joint (white dots) and the PAZ (white dash-dot lines).

The following major features could be noted for AW: 1) worsened properties were obtained compared to the ones of the as-received BM (see *Table 1*) characterized by a remarkably shortened elongation at break (3.6%), an apparent lower stiffness (78 GPa), and a seemingly early plastic behavior (731 MPa); 2) the β_m joint core (WL+TMAZs) appeared more prone to deform than the neighboring $\alpha+\beta_m$ microstructures (HAZs); 3) significant strain heterogeneities existed within the β_m joint core in the initial linear stage; 4) a shift in the position of the maximum strain from the forging to the oscillating TMAZ occurred around 0.8% of macroscopic strain which corresponds to the end of the initial linear σ/ε stage; 5) a sudden decrease in the share of the deformation handled by the BM appeared around 1.5% of macroscopic elongation accompanying a noteworthy work hardening and an extensive strain localization in the oscillating TMAZ; 6) failure occurred ultimately in the oscillating side close to the WL/TMAZ border.

a)



b)

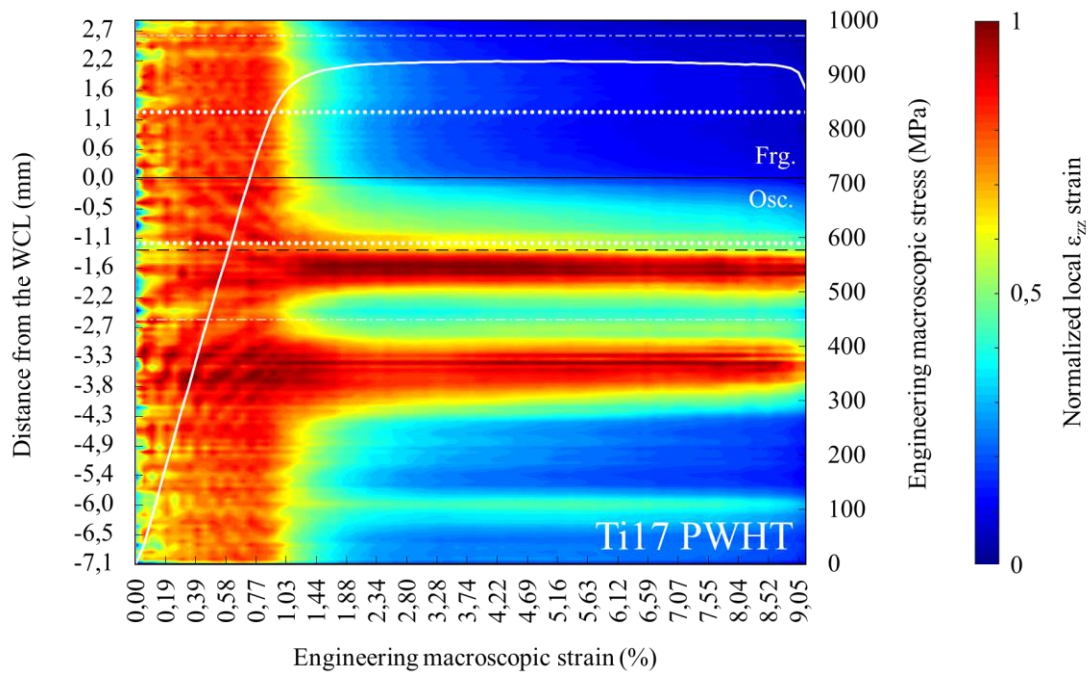


Figure 8 : Intensity maps of the spatio-temporal graphs depicting the evolution of the ϵ_{zz} strain localization across the weld center line (WCL) while loading combined with the engineering stress/strain curves in white solid line for a) the as-welded (AW) and b) post-weld heat treated (PWHT) Ti17 samples; the solid and dashed black lines indicate

the positions of the WCL and the final fracture respectively; the forging side (Frg.) corresponds to the part of the intensity maps above the WCL and inversely for the oscillating side (Osc.); the white dots and dash-dot line indicate the limits of the joint and the Process Affected Zone respectively.

A similar analysis conducted on PWHT revealed the following main features: 1) forming back the Widmanstätten $\alpha+\beta$ microstructure across the weld permitted to recover an elongation at break (9.2%), a stiffness (100 GPa) and a yield stress at 0.2% offset (884 MPa) in the order of magnitude of the ones specified for the as-received BM; 2) a rather homogeneous response was found across the assembly in the linear stage up to 1% of macroscopic elongation; 3) plastic deformation occurred in the whole structure including the transformed WL; 4) plastic strain localized in two preeminent zones with one sitting in the former oscillating HAZ leading ultimately to failure in the latter.

The previously depicted evolution of the tensile behavior across AW showed that the gradients of microstructure affected considerably the local mechanical behavior. Hence the use of local sub-analysis was proposed in this study to eventually identify the inherent differences in the tensile responses (see protocol in section 4.2). To do so numerical gauges were symmetrically set on either side of the weld center line corresponding to the positions of the WL ($|z| \leq 200 \mu\text{m}$), the TMAZs ($200 \leq |z| \leq 1200 \mu\text{m}$), and the HAZs ($1200 \leq |z| \leq 2600 \mu\text{m}$). The resulting local true stress/strain curves (truncated at the onset of macroscopic necking) were then compared to each other in *Figure 9* using the following indicators: the longitudinal stiffness, the yield stress at 0.2% offset and the work-hardening exponent (ranging from the yield point at 0.5% offset to the onset of necking). Such data were used here in a qualitative way for

identifying the eventual contributions of the gradients of microstructure, SIM transformations and/or micro-mechanical effects to the local tensile behavior. Thus these data should not be assimilated as intrinsic mechanical properties of the assemblies for Representative Elementary Volume (REV) conditions are not verified and combined complex mechanisms were part of the tensile responses. The original true stress/strain curves are provided in Appendix A.

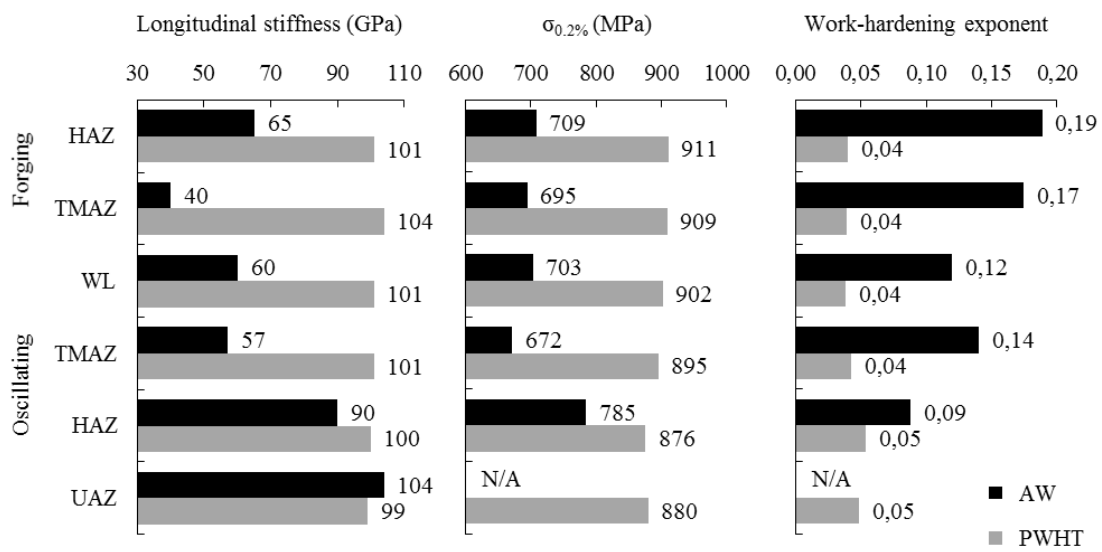


Figure 9 : Local main tensile properties of each joint macro-zones (i.e. the WL, TMAZs, HAZs) obtained from their respecting true stress/strain curves truncated at the onset of macroscopic necking for the as-welded (AW) and the heat treated (PWHT) Ti17 samples; the Unaffected Zone (UAZ) represents the material far from the weld (i.e. $z < -3$ mm); the work-hardening exponent was obtained ranging from the yield point at 0.5% offset to the onset of necking; the original true stress/strain curves are provided in Appendix A.

The analysis over the macro-zones of the AW sample revealed the following features: 1) a loss in the longitudinal stiffness in the PAZ characterized by a noteworthy

local drop in the forging TMAZ; 2) a remarkable asymmetry between the oscillating and the forging parts, the latter seeming to be more affected by the process regarding the three indicators considered; 3) a higher yield stress and lower work-hardening in the WL than in the surrounding β_m TMAZs; 4) close investigations at the apparent yield strengths ($\sigma_{0.05\%}$) in both TMAZs revealed similar values but different hardening rates resulting in a higher $\sigma_{0.2\%}$ in the forging side; 5) an overmatching effect of the unaffected material. The sub-analysis on the macro-zones of the PWHT sample showed that quite homogeneous tensile properties were recovered across the former joint. Yet one could still note an overall slight loss in stiffness (-5%) from the initial as-received base material (AW UAZ) and a minor overmatch of the transformed joint compared to the rest of the heat treated assembly.

The position of the fracture within the plastically affected microstructure and the corresponding fractographies by SEM of the AW sample are shown in *Figure 10*. The presence of numerous slip bands (markers ①) revealed that both the WL and the forging TMAZ endured significant plastic deformations. Moreover one could note the presence of entangled linear irregularities (markers ②) identified by the authors in [39] as traces of a probable precipitation of α'' plates. The fractographies in *Figure 10b* exhibited two population of dimples (small and large) coexisting with seemingly cleavage-like features characterized by deep steps (*Figure 10c-d*) and apparent tongues and rivers (marker ④ and ⑤ respectively). Significant changes in the propagation direction of the main crack were visible with a noteworthy transition from profound to shallow dimples ultimately revealing serpentine glide traces on the edges of the sample (marker ③). The presence of a second crack might also be probable (the top right corner).

Similar investigations were conducted on the fracture of the heat treated sample PWHT, the corresponding OM observations and fractographies are shown in *Figure 11*.

The micrograph showed that the main crack seemed to have propagated within the former oscillating HAZ through a band of severely plasticized large prior- β grains (marker ①); sharp changes in the propagation direction were also noted. The fractographies in *Figure 11b-d* revealed remarkable changes in the propagation direction across the fracture surface; the latter was mainly composed of dimples (marker ③). Few local cleavage features could be observed with characteristic facets and rivers (marker ④). Coarse cleavage resembling a typical failure at the α grain boundary (α_{GB}) was also identified (marker ②) [12].

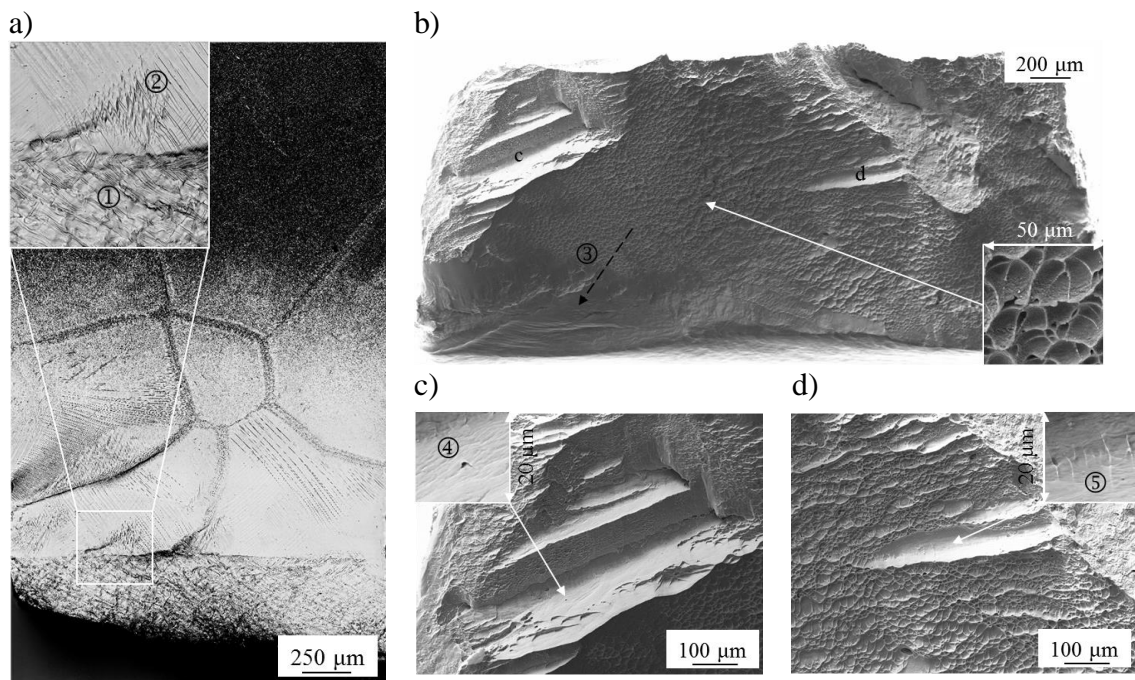


Figure 10 : Fractographies of the as-welded Ti17 sample showing a) OM of the deformed microstructure exhibiting numerous slip bands in the WL (marker ①) and traces of α'' precipitation in the TMAZ (marker ②) with $\langle x \rangle$ pointing east and $\langle z \rangle$ pointing north; b) SEM observations and local zooms c)-d) of the crack surface revealing dimples (marker ③) coexisting with cleavage-like features (markers ④ and ⑤) with $\langle x \rangle$ pointing east and $\langle y \rangle$ pointing south.

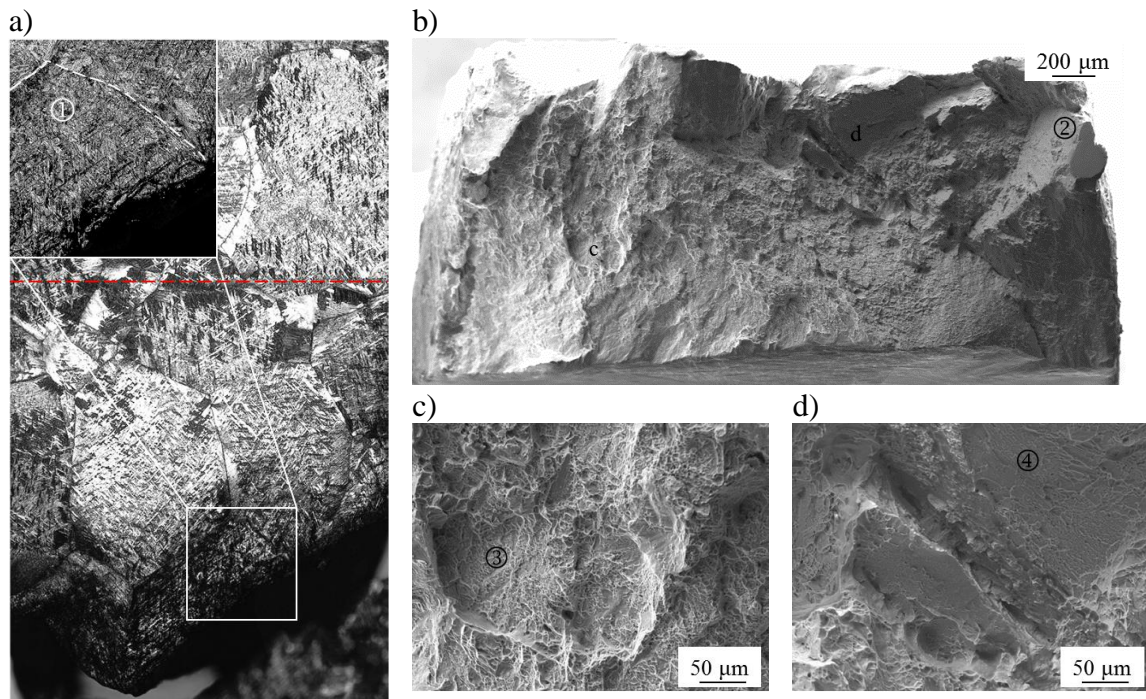


Figure 11 : Fractographies of the heat treated Ti17 sample showing a) OM of the deformed microstructure exhibiting an apparent intragranular fracture (marker ①) with $\langle x \rangle$ pointing east and $\langle z \rangle$ pointing north, the red dashed line highlights the position of the transformed WL; b) SEM observations and local zooms c)-d) of the crack surface revealing mainly dimples (marker ③) and little cleavage (markers ② and ④) with $\langle x \rangle$ pointing east and $\langle y \rangle$ pointing south.

The investigations conducted in this paper revealed that the microstructural changes induced by LFW had considerable impacts on the tensile behavior of the β -metastable Ti17. Indeed one should recall that the process resulted in severe gradients of thermo-mechanical loads within the welded parts leading to: 1) a complete $\alpha \rightarrow \beta$ phase

transformation in the joint core ($|z| \leq 1.2$ mm) with a remarkable grain refinement at the very center of the weld ($|z| \leq 0.2$ mm); 2) a gradual partial shrinkage of the hardening α precipitates further from the heat source ($1.2 \leq |z| \leq 2.6$ mm); 3) a $\beta_{\text{transformed}} \rightarrow \beta_{\text{metastable}}$ phase transformation upon fast cooling following the end of the oscillations. As a result the present authors proposed to conduct a succinct crystallographic analysis to highlight the contribution of local microstructural state to the macroscopic elastic properties of the Ti17 presently investigated. The subsequent plots of the tensile stiffness along various crystal directions for a β_m lattice, as well as for a simulated Widmanstätten microstructure are shown in *Figure 12*. The latter was obtained by determining the α orientations of one cluster of three self-accommodating intragranular α laths that obey the burgers orientation relationship with the parent β matrix [40]; a phase volume fraction similar to the one of as-received BM was set (80% α ; 20% β). The elastic tensor components used for this analysis are listed in *Table 2*.

Table 2 : Elastic stiffness components C_{ij} in [GPa] in Voigt matrix representation at room temperature for the equilibrium Ti17 β lattice, LCB Ti-alloy β_m lattice and commercially pure (CP) Ti-alloy α lattice determined in [41], [42], [43] respectively; E_{iso} is the isotropic Young's modulus determined from the Voigt-Reuss-Hill approximation.

Phase	β	β_m	α
Ti-alloy	Ti17	LCB	CP
C_{11}	167	138	162
C_{33}			181
C_{12}	115	102	92
C_{13}			69
C_{44}	44	43	47

C_{66}			35
E_{iso}	100	84	115
Ref	[41]	[42]	[43]

The lattice data (see *Table 2*) highlighted the fact that a loss in volume fraction of the α phase would necessarily lead to a decrease in the isotropic elastic modulus. Such a dissolution of the cluster of α laths would also result in enhanced local stiffness variations inherited from the anisotropic behavior of the β phase. Furthermore, the growth of the β matrix at the expense of the α phase at high temperatures ($T^{\circ} > 700$ °C) causes a decrease in fraction of the $\beta_{\text{stabilizing}}$ elements [36] which was shown to remarkably affect the components of the elastic tensor of the Ti BCC lattice [44]. These findings as well as the elastic properties of the retained β_m lattice measured in [42] for the LCB Ti-alloy are corroborating the global decrease and the remarkable local variations in stiffness identified in the as-welded sample. Yet, given the preferred orientation of the β crystallites in the WL aligning one $\langle 112 \rangle$ direction with the forging axis $\langle z \rangle$ during LFW [9], [10], the elastic stiffness components of this β_m phase would imply to have an estimated longitudinal stiffness in the WL about 88 GPa. This value is 45% higher than the one measured here (60 GPa in *Figure 9*) which could be imputed to the differences in chemical compositions of the β_m phases of the Ti17 and the LCB Ti-alloys.

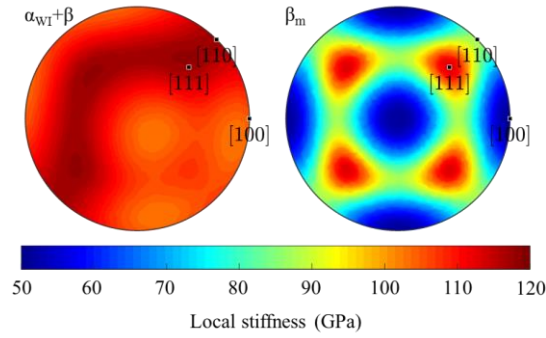


Figure 12 : Variation of the elastic modulus depending on the crystallographic directions according to the elastic constants listed in Table 2 for a β_m lattice and for a simulated β grain hardened by three self-accommodating intragranular α laths (α_{w1}); the Burgers orientation relationship for the $\beta \rightarrow \alpha$ precipitation is $\{0001\}_\alpha // \{110\}_\beta / \langle 11\bar{2}0 \rangle_\alpha // \langle 1\bar{1}1 \rangle_\beta$ and the three chosen α variants ensured the alignment of their $[11\bar{2}0]$ directions and a 60° angle between their (0001) planes [40]; each cluster possible would result in local minimum and maximum stiffness of 103 and 118 GPa respectively; the positions of the $[100]$, $[110]$, and $[111]$ directions of the parent β orientation are also plotted.

In addition to the local variations in stiffness that could be attributed to the anisotropic elastic properties of the BCC β_m phase, a remarkable asymmetry was also noted in the tensile behavior of the as-welded sample on either side of the weld center line. Indeed, the forging part appeared to be more affected by LFW than the oscillating part through lower stiffness and yield strength but higher hardening capacity in the former compared to the latter (see Figure 9). Such differences could be imputed to the presence of asymmetrical thermo-mechanical loads during the process as shown in Figure 13. This might have affected differently both welded parts in terms of fraction of remaining α phase and/or the local triggering stress for the SIM transformation. In fact,

the latter was found to be responsible for: 1) lowering the apparent yield strength when forming below the true yield strength of the parent phase; 2) resulting in a significant work-hardening by slip-length reduction and α'' reorientation [36], [45]–[47]. Thus, the forging side may have experienced an early and gradual SIM transformation that worsened both the local stiffness and the yield stress but resulted in a significant α'' precipitation (see marker ② in *Figure 10*) hardening the microstructure. The probably lower α'' precipitation in the oscillating TMAZ might have favored strain localization in this macro-zone which ultimately cracked. In addition to that the grain refinement in the WL might have resulted in hindering the SIM transformation in the refined crystallites compared to the neighboring TMAZs as: 1) fine grains impede the shape change accommodation of the martensitic plate [48]; 2) the formation of subgrains with low dislocation densities [19] limits the presence of nucleation sites [49]; 3) the migrating boundaries enhanced the diffusion and chemical homogenization [50], thus reducing the martensitic start temperature [36]. These microstructural features directly affect the triggering stress for the SIM transformations which was probably limited in the refined WL in favor of the rest of the joint resulting in slightly higher stiffness and yield strength in the former.

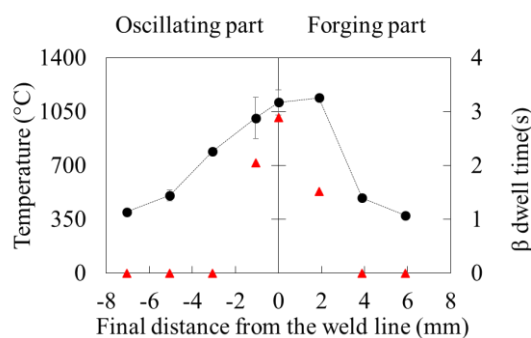


Figure 13 : Local temperature maxima measured by the thermocouples (black dots) in dependence on the final distance from the weld center line after axial shortening; the

local dwell times in the β domain experienced during the process are represented by the red triangles [9].

The strain localization in the oscillating TMAZ led ultimately to failure characterized by quasi-cleavage features consisting of a mixture of micro-voids and facets. The formation of dimples could be imputed to crack nucleation at the β/α boundaries and/or at the intersections of intense slip bands [51]. The heterogeneous deformation induced by the sharp microstructure refinement at the WL/TMAZ border might be responsible for cleavage and/or intergranular fracture. Similar fracture features were observed for an as-welded LFW Ti17 joint [20], however the authors in [21] reported solely a ductile transgranular fracture in the as-welded LFW Ti5553 joint. Higher density of ω_{athermal} particles forming in the latter might have deflected the crack from the WL/TMAZ border in favor of a regular transgranular fracture [52].

The investigations conducted on the samples after PWHT showed that a rather homogeneous elastic behavior was recovered in the whole assembly. Such an improvement from the as-welded properties are directly related to the reprecipitation of the hardening α phase in the form of self-accommodating α_{WI} clusters as shown in *Figure 12*. However the former oscillating HAZ still appeared as a weak point after PWHT due to a significant plastic strain localization ultimately leading to failure. Indeed the coarser prior- β grains in this macro-zone (see *Figure 7*) might have resulted in a local weakening due to large α plates at the prior- β grain boundaries [12]. Moreover the activation of restoration mechanisms in the joint during the PWHT might have lowered the density of intragranular dislocations; the latter being desirable for a precipitation of fine entangled α_{WI} laths [12]. The slight decrease in stiffness from the as-received material might be due to a probable higher fraction of β matrix. The heat

treated samples exhibited mixed fracture modes of ductile intragranular and intergranular crack propagations mainly consisting of large dimples and cleavage rivers on grain facets. This fracture mode is typical of β annealed lamellar microstructures [12], [52]–[54]; to the authors knowledge no similar transformed β -metastable Ti-alloys LFW joints was found in the literature for comparison purposes. The difference of approximately ten percent (-10%) in the stiffness and/or the yield stresses measured in the base material compared to the ones provided by the manufacturer could be imputed to a sample size effect.

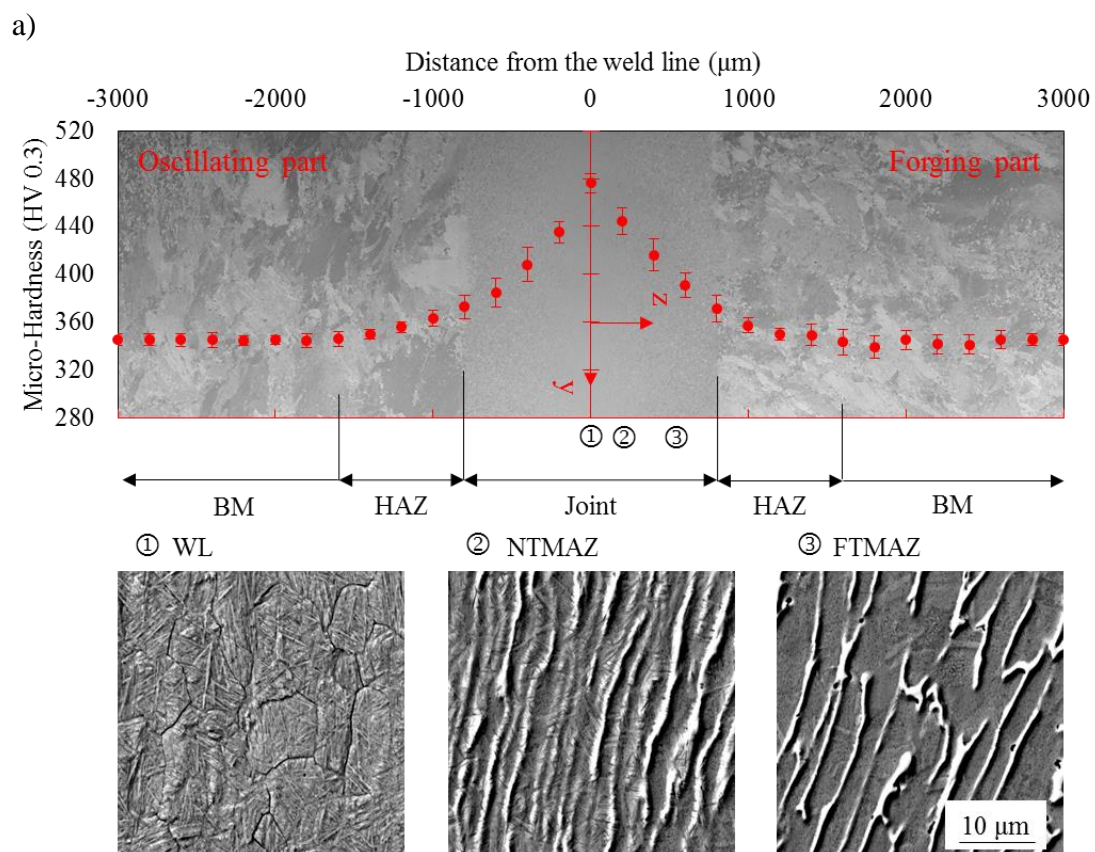
3.2. Ti6242 LFW joint

3.2.1. Microstructure

Previous investigations focused on identifying the mechanisms responsible for the microstructural changes in a near- α Ti6242 LFW joint with a starting fully-equiaxed microstructure [10]. The microstructures and hardness properties of the joint before and after the PWHT are displayed in *Figure 14*.

The different thermo-mechanical loads locally experienced by the material during LFW had remarkable effects on the as-received configuration deeply affecting the microstructures of the latter and the resulting mechanical properties. Similarly to the Ti17, four distinct macro-zones were identified as being affected by the process: the Welding Line (WL ; $|z| \leq 100 \mu\text{m}$) made of highly textured entangled martensitic α' plates precipitated within fine prior- β subgrains ($\langle 0001 \rangle$ direction almost aligned with the transversal direction $\langle x \rangle$ and the $\langle 11\bar{2}0 \rangle$ direction aligned with the oscillation direction $\langle y \rangle$); the Near Thermo-Mechanically Affected Zone (NTMAZ ; $100 \leq |z| \leq$

350 μm) consisting of a mix of $\alpha_{\text{secondary}}$ fragments and martensitic α' plates formed across strata of highly deformed former α nodules and retained “Ghost” β matrix; the Far Thermo-Mechanically Affected Zone (FTMAZ ; $350 \leq |z| \leq 800 \mu\text{m}$) exhibiting just deformed former α nodules refined by $\alpha_{\text{secondary}}$ precipitates that share clear orientation relationships with the adjacent β matrix; and the Heat Affected Zone (HAZ ; $800 \leq |z| \leq 1600 \mu\text{m}$) indistinguishable from the base material but displaying a slightly affected hardness. The Process Affected Zone (PAZ ; $|z| \leq 1600 \mu\text{m}$), includes all the macro-zones depicted previously.



b)

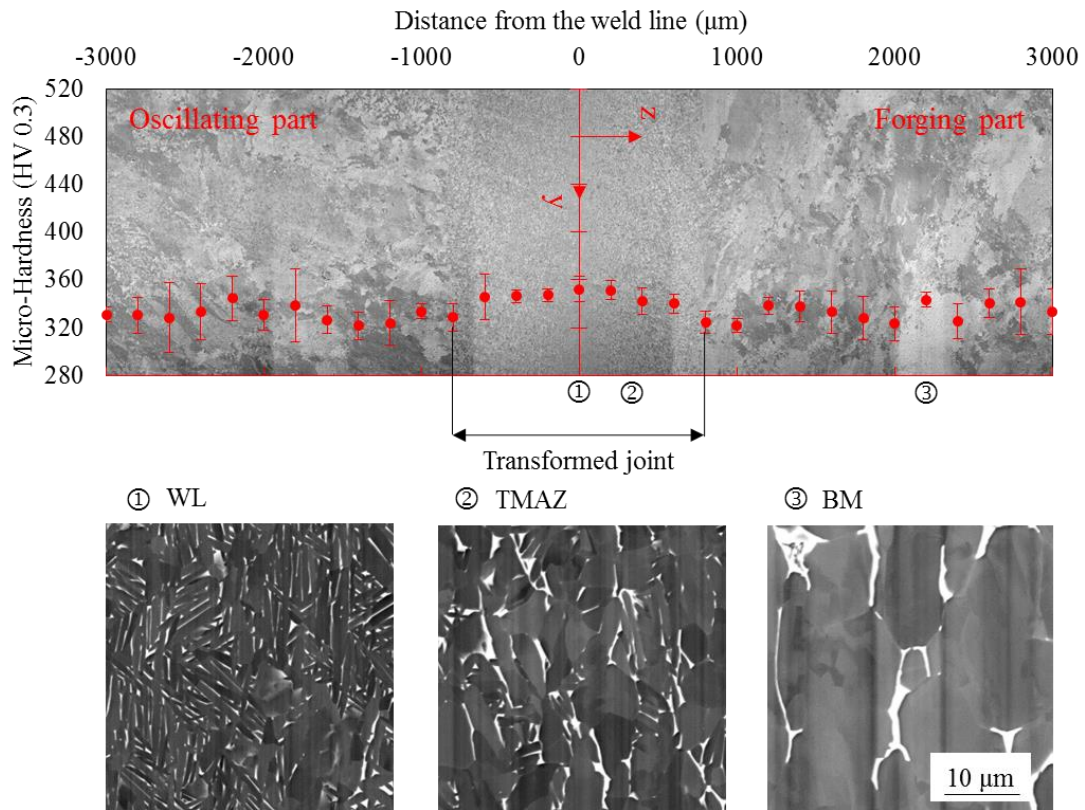


Figure 14 : Combined data from OM observations under polarized light and the corresponding local hardness across the Ti6242 LFW joint in a) the as-welded (AW) configuration and b) after a Post-Weld Heat Treatment (PWHT); zooms obtained by SEM on the Welding Line (WL), the near and far Thermo-Mechanically Affected Zone (NTMAZ and FTMAZ), and the base material (BM) after the heat treatment are also provided; $z=0$ is set at the weld center line.

This significant microstructure refinement from the initial fully-equiaxed $\alpha+\beta$ mixture by phase transformations and/or continuous dynamic recrystallization resulted in a notable hardening and a consistent weld overmatch effect. Such microstructural changes might have affected considerably the local mechanical behavior and durability of the joint. Indeed the authors in [37] showed, through an extensive study, that the mechanical behavior of the $\alpha+\beta$ Ti64 (10 v% β) is remarkably dependent on the Heat

Treatment and Quenching (HTQ) temperature impacting at least: the stiffness, the tensile strength and the work-hardening capacity. This was mostly attributed to the $\alpha \rightarrow \beta_t$ phase transformation which leads to a decrease in the fraction of $\beta_{\text{stabilizing}}$ elements in the β_t matrix (β_{lean} in place of β_{rich}) ultimately transforming upon quenching either in: hexagonal α' , orthorhombic α'' , metastable β_m , and/or cubic β depending on the volume fraction of β_t [55]. The α' and/or α'' precipitation from the β_t matrix was shown to considerably increase the tensile strength as well as the work-hardening capacity while slightly lowering the tensile stiffness. Yet retaining a 15 v% β_m matrix by HTQ from 800 °C leads to a significant decrease in the apparent yield stress and stiffness due to a SIM transformation occurring during loading; the latter being also identifiable by an enhanced work-hardening capacity. The PWHT consisting of an $\alpha + \beta$ annealing followed by ageing resulted in: 1) homogenizing the β phase fractions and micro-hardness values across the assembly; 2) a gradual microstructure refinement from the HAZ to the WL; 3) maintaining a fully-equiaxed microstructure in the rest of the assembly.

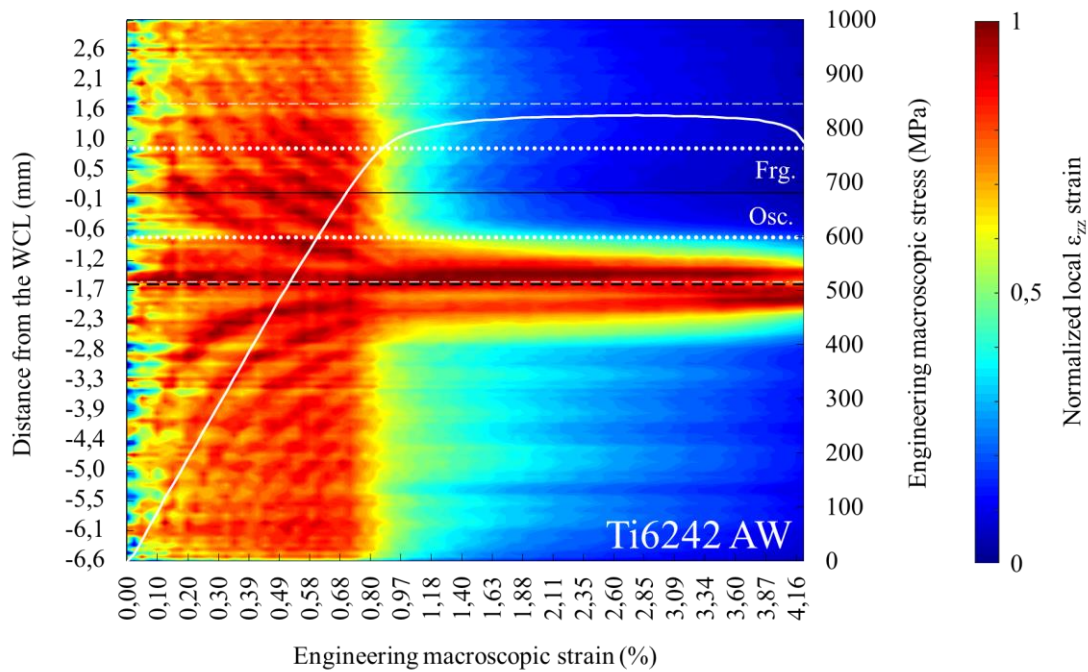
3.2.2. *Micro-tensile test response*

Monotonic micro-tensile tests were performed in the same manner than on the TI17 on the as-welded (AW) and the heat treated (PWHT) assemblies. The PAZ and the WL+TMAZs constitute respectively 30% and 15% of the total gauge length L_0 ($L_0 \approx 10$ mm). The macroscopic engineering stress/strain curves (solid white) and the normalized spatio-temporal graphs of the local ε_{zz} strain during the tests are plotted in *Figure 15*. The approximate $\langle z \rangle$ positions of the WL (black solid line) and the final crack paths (black dashed line) are also provided along with the limits of the joint (white dots) and the PAZ (white dash-dot lines).

The main outcomes of the tensile behavior of Ti6242 AW are listed as followed:

- 1) the stiffness and yield stress at 0.2% offset (101 GPa and 784 MPa respectively) were in the order of magnitude of the as-received BM (see *Table I*), however a clear drop in the elongation at break could be noted (-65%);
- 2) a slightly higher displacement was observable within the joint during the macroscopic linear stage compared to the unaffected material;
- 3) the hard joint (WL+TMAZs) appeared to not contribute significantly to the macroscopic deformation past the apparent yield point compared to the seemingly plasticized HAZs and BM;
- 4) a remarkable strain localization was identified in the oscillating HAZ which ultimately cracked.

a)



b)

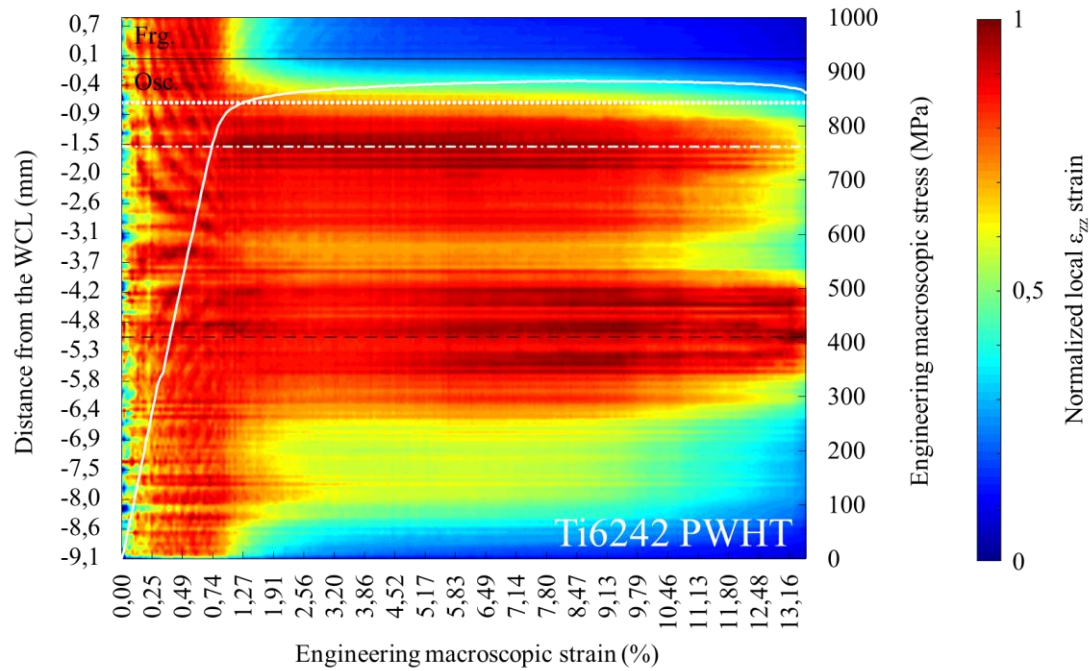


Figure 15 : Intensity maps of the spatio-temporal graphs depicting the evolution of the ϵ_{zz} strain localization across the weld center line (WCL) while loading combined with the engineering stress/strain curves in white solid line for a) the as-welded (AW) and b) post-weld heat treated (PWHT) Ti6242 samples; the solid and dashed black lines indicate the positions of the WCL and the final fracture respectively; the forging side (Frg.) corresponds to the part of the intensity maps above the WCL and inversely for the oscillating side (Osc.); the white dots and dash-dot line indicate the limits of the joint and the Process Affected Zone respectively.

The transposable investigations conducted on the heat treated Ti6242 assembly revealed that: 1) the decomposition of the $\alpha' + (\alpha'')$ martensitic laths into an equilibrium $\alpha + \beta$ microstructures resulted in a remarkable improvement of the macroscopic elongation at break (14%) and yield stress at 0.2% offset (829 MPa); 2) the stiffness was slightly increased (105 GPa) compared to the AW configuration; 3) homogeneous displacement were recorded across the assembly during the linear stage; 4) the plastic

deformation seemed to solely occur outside of the transformed joint (i.e. in the unaffected material); 5) no particular strain localization was noted any longer; 6) failure ultimately occurred in the unaffected material (i.e. far from the joint).

Given the discrepancies in the local displacements during loading, a complementary analysis was conducted to account with the gradients of microstructures across the assemblies (see *Figure 16*). A procedure similar to the one performed on the Ti17 was proposed here: the stiffness, the yield stress and the work-hardening capacity were determined (when applicable) from the local true stress/strain curves truncated at the onset of macroscopic necking (see protocol in section 4.2). The numerical gauges were symmetrically set on either side of the weld center line corresponding to the positions of the following macro-zones: the WL ($|z| \leq 100 \mu\text{m}$), the NTMAZs ($100 \leq |z| \leq 350 \mu\text{m}$), the FTMAZs ($350 \leq |z| \leq 800 \mu\text{m}$), and the HAZs ($800 \leq |z| \leq 1600 \mu\text{m}$). Since the REV conditions were not fulfilled, these mechanical behavior indicators would solely be used for comparison purposes between the AW and PWHT samples. The original true stress/strain curves are provided in Appendix B.

One could observe from the data gathered in *Figure 16* that, besides exhibiting a significant overmatch, the AW joint (WL+TMAZs) is characterized by a ten percent decrease in stiffness compared to the as-received unaffected material. This loss appeared not to be dependent on the local microstructure nor the weld side. However, a noteworthy asymmetry was identified between the forging and the oscillating parts regarding the yielding of their respective FTMAZs and HAZs. Indeed these macro-zones seemingly plasticized solely in the oscillating work-piece. In addition to that the HAZ of the latter was characterized by decreases in stiffness and in yield strength (–10% and –5% respectively) compared to the adjacent unaffected material (UAZ) despite exhibiting supposedly similar microstructures.

The analogous studies conducted on the PWHT sample showed that the overmatching effect in the joint was drastically lowered after the heat treatment through an apparent plastic behavior in the latter as well as in the rest of the assembly; yet slightly higher strengths were locally noted in the initially refined zones. The stiffness was also homogenized across the assembly to a value similar to the one of the as-received base material after ageing in the $\alpha+\beta$ domain. Moreover the forging HAZ did not constitute a particular soft point any longer since the yield strength and the work-hardening capacity were henceforth comparable with the adjacent heat treated base material (UAZ). Yet the asymmetry in yield strength between the TMAZs of the forging and the oscillating part was still present and the PWHT seemed to have caused a slight hardening of the base material (+3%). Due to the position of the weld center line within the sample, no data were acquired in the forging HAZ.

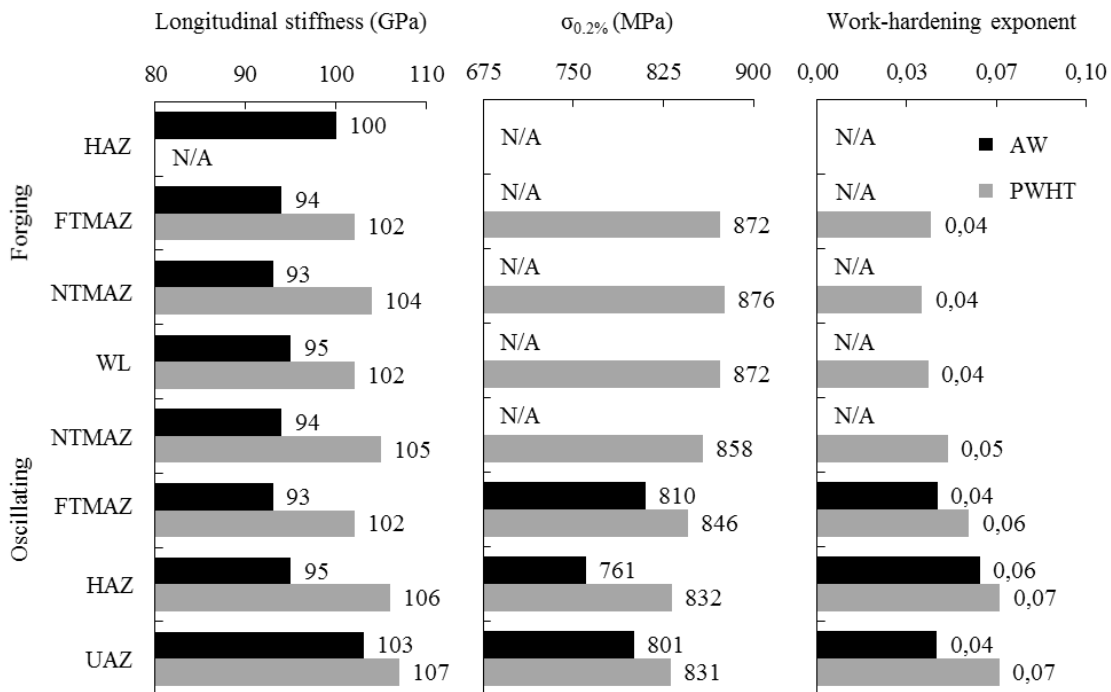


Figure 16 : Local main tensile properties of each joint macro-zones (i.e. the WL, NTMAZs, FTMAZs, and HAZs) obtained from their respecting true stress/strain curves

truncated at the onset of macroscopic necking for the as-welded (AW) and the heat treated (PWHT) Ti6242 samples; the Unaffected Zone (UAZ) represents the material far from the weld (i.e. $z < -3$ mm); the work-hardening exponent was obtained ranging from the yield point at 0.5% offset to the onset of necking.

An OM observation of the position of the fracture within the AW sample and the corresponding fractographies of the crack surface obtained by SEM are provided in *Figure 17*. The micrograph in *Figure 17a* revealed that the surface microstructure past the FTMAZ (i.e. starting at 1 mm from the WL) was topographically affected after loading indicating a probable intense plastic deformation in these zones; no traces of such features were observable within the refined macro-zones (i.e. WL, NTMAZs and FTMAZs). The fractography in *Figure 17b* and the zooms in specific zones in *Figure 17c-d* revealed the presence of small dimples coexisting with a seemingly cleavage of the α nodules. In addition to that one could notice sharp crack deflection characterized by apparent large grain facets (marker ①), deep steps (marker ②), and a probable second crack initiation (marker ③). Analogous investigations on the PWHT sample are displayed in *Figure 18*. The corresponding observations showed that, despite failing far from the weld center line, topographical signatures of an extensive plastic behavior were identifiable in the transformed FTMAZ/HAZ. The resulting crack surface was characterized by slant and flat fractures on the top/bottom edges and center of the cross-section respectively; mainly dimples and little cleavage through the α nodules were reported.

a)

b)

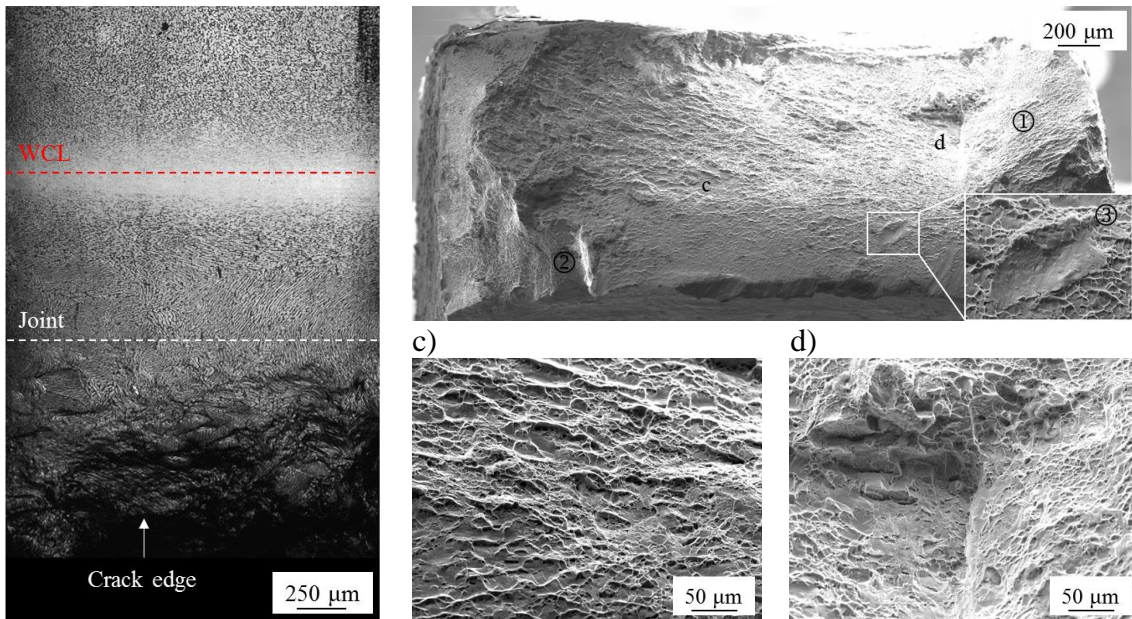
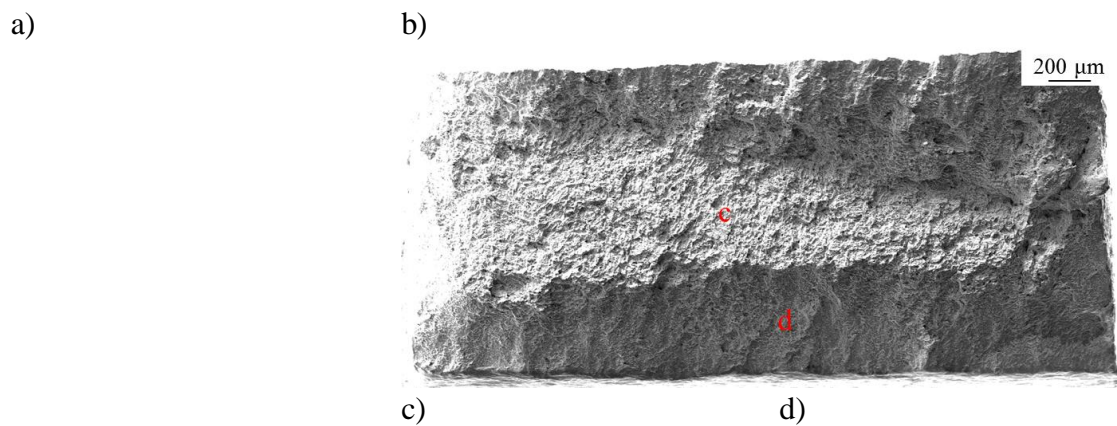


Figure 17 : Fractographies of the as-welded Ti6242 sample showing a) OM of the deformed microstructure exhibiting an extensive strain localization outside the refined joint with $\langle x \rangle$ pointing east and $\langle z \rangle$ pointing north (the red and white dashed lines represent the positions of the weld center line and the joint limit respectively) ; b) SEM observations and local zooms c)-d) of the crack surface revealing small dimples, cleavage of the α nodules, sharp crack deflections (markers ① and ②), and a probable second crack opening (markers ③) with $\langle x \rangle$ pointing east and $\langle y \rangle$ pointing south.



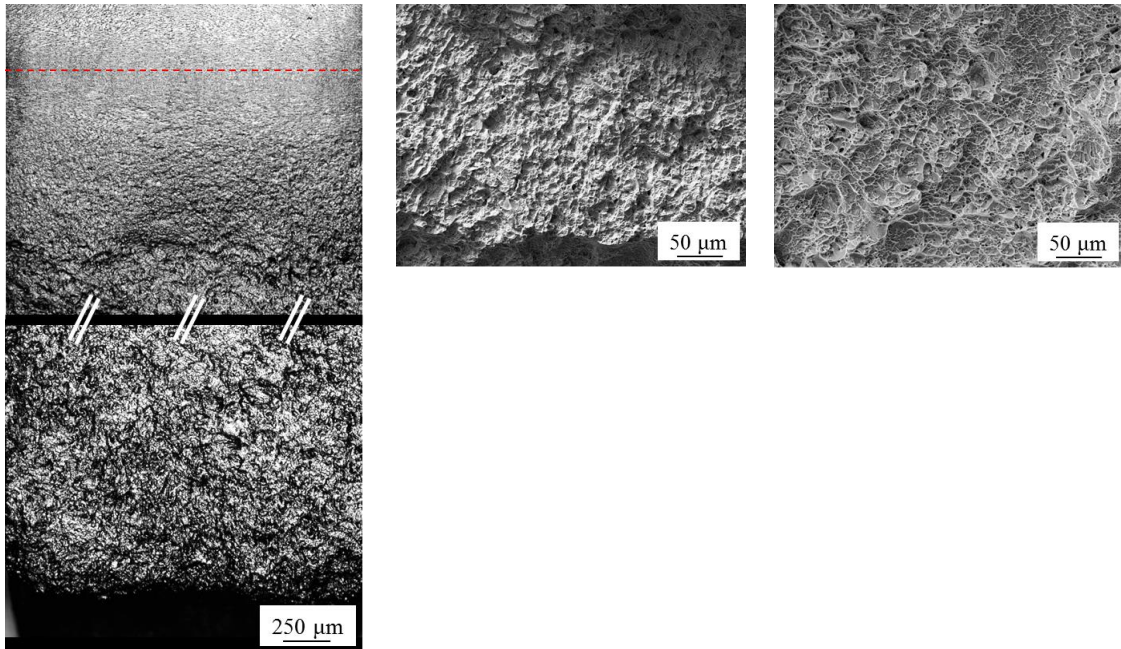


Figure 18 : Fractographies of the heat treated Ti6242 sample showing a) OM of the deformed microstructure within the joint (top) near the weld center line in red dashed line and, far from the joint, near the final crack (bottom) with $\langle x \rangle$ pointing east and $\langle z \rangle$ pointing north; b) SEM observations and local zooms c)-d) of the crack surface revealing a flat surface at the center neighbored by slant fractures both being mainly composed of dimples and little cleavage through the α nodules.

The micro-tensile tests performed in this study confirmed that the remarkable microstructural changes experienced within the LFW Ti6242 joint led to consistent discrepancies in the local mechanical behaviors. These discrepancies are directly linked to the gradients of thermo-mechanical loads experienced across the weld during the process resulting in logical gradients of microstructural changes and refinements. Indeed previous investigations detailed in [10] showed that the microstructure refinement in the joint was due to an extensive $\alpha \rightarrow \beta_t$ transformation in this zone. Such a transformation led to different local reprecipitation from the β_t zones upon cooling depending on their local chemical composition: 1) $\beta_t \rightarrow \alpha'$ in the WL due to the high

temperatures and migrating boundaries that enhanced the diffusion and chemical homogenization; 2) $\beta_t \rightarrow \alpha_s + \beta + (\beta_m)$ in the FTMAZ caused by a limited diffusion of the $\beta_{\text{stabilizing}}$ elements from the initial β matrix to the whole β_t area; 3) a mix of the previously depicted transformations in the NTMAZ with a probable presence of α' martensitic plates within the retained “Ghost” β . In the preliminary microstructural investigations no microstructural changes were identified in the HAZ compared to the as-received BM. However recent SEM micrographs shown in *Figure 19* revealed that the β matrix in the BM was actually initially hardened by fine α_s platelets; the latter were absent in the HAZ. The apparent dissolution of these α_s platelets in the HAZ caused an increase (+40%) in the area fraction of the β matrix by contrast distinction from eight percent in the BM to eleven percent in the HAZ.

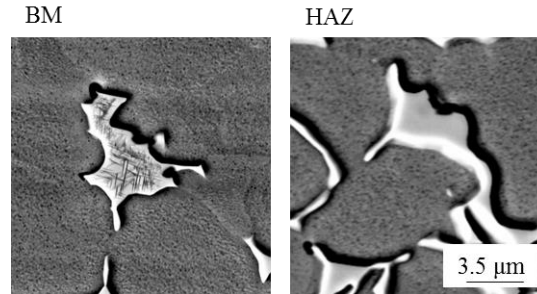


Figure 19 : SEM observations of the β matrix in the as-received Base Material (left) and the as-welded Heat-Affected Zone (right) showing the clear loss of the hardening α_s platelets in the β matrix of the HAZ after welding.

The authors in [56] showed that quenching a Ti-alloys from the β -domain would result in a significant loss of stiffness depending on the fraction of $\beta_{\text{stabilizing}}$ elements dissolved in the bulk (see *Figure 20*). As a result, retaining an α' martensitic microstructure in place of an equilibrium α phase would inevitably lead to a noteworthy

decrease in Young's modulus. Such a mechanism was thought to be responsible for the lower stiffness measured in the WL compared to the as-received BM.

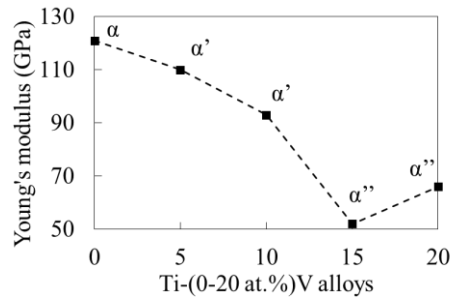


Figure 20 : Evolution of the isotropic Young's modulus of the martensitic phases retained by quenching from the β -domain for different contents of $\beta_{stabilizing}$ element in Ti-(0-20 at.%)V alloys [56].

The apparent lower chemical homogenization further from the WL probably led to the presence of soft α'' and/or β_m phases in the rest of the joint (i.e. NTMAZs, FTMAZs, and HAZs), this might have lowered as well the local stiffness. Consequently, repartitioning the $\beta_{stabilizing}$ elements during the PWHT into equilibrium $\alpha+\beta$ microstructures permitted to homogenize the stiffness across the assembly back to values similar to the one of the as-received BM. In both AW and PWHT cases, the presence of multiple α variants prevented the joint core (i.e. WL, NTMAZs and FTMAZs) from exhibiting significant stiffness variations from one macro-zone to the other.

The microstructure refinement caused a noteworthy weld overmatch, yet solely the oscillating side appeared to be prone to reach an apparent yielding point. Unlike in the Ti17, the temperature measurements conducted during welding and reported in [10] did

not provide evidence of any asymmetrical heat flux that would corroborate the difference in mechanical behavior observed here between both work-pieces. However, the microstructural investigations detailed in [10] showed that the oscillating part actually experienced an enhanced recrystallization compared to the forging part. This might have resulted in slightly higher local temperatures and an enhanced chemical diffusion which caused the differences in mechanical behavior identified here in the AW configuration.

Despite showing a fifty percent decrease in grain size compared to the as-received fully-equiaxed microstructure and no weakening texture [10], the as-welded oscillating FTMAZ exhibited a rather low yield strength combined with a noteworthy work-hardening capacity. Such a behavior was identified in metastable Ti64 microstructures as resulting from the occurrence of a SIM transformation within a β_m matrix [37], [55]. The dissolution of the α_s platelets in favor of the β matrix in the oscillating HAZ combined with a local altered strength and a notable work-hardening capacity would indicate that this macro-zone also experienced the $\beta_m \rightarrow \alpha$ transformation. Yet the extensive strain localization in the HAZ and the consistent limited macroscopic elongation might be most likely due to an increase in slip length resulting from the local dissolution of incoherent $(\text{Ti,Zr})_5\text{Si}_3$ and coherent Ti_3Al particles. These two precipitation hardening mechanisms, initially present in the as-received BM, are known to effectively prevent the occurrence of easy slip over long distances through former α colonies [12], [57]; their dissolution would inevitably lead to an early strain localization and a limited macroscopic elongation. The dislocation pile-up at the boundaries of these α colonies in the HAZ may have resulted in multiple early crack nucleation sites causing the subsequent quasi-cleavage fracture. The anisotropic thermal expansion of

the α colonies [58] could have also led to internal damage resulting from the thermal shock experienced in the HAZ, thus weakening the latter.

In addition to a homogenized stiffness, subjecting the assembly to a PWHT led to a smooth microstructure refinement across the joint with lamellar $\alpha+\beta$ in the WL and gradually refined α nodules in the TMAZ; the fully-equiaxed microstructure of the BM was preserved. These gradients of microstructure are visible in the form of a remaining slight weld overmatch. However one could still note a significant asymmetrical behavior as TMAZ of the oscillating side appeared to be softer than the one of the forging side. This might be resulting from the presence of finer microstructures in the latter. Furthermore ageing at 635 °C for 8h might have favored an enhanced precipitation of Ti_3Al particles responsible for the slight hardening of the BM after the PWHT. These microstructural changes resulted in a homogeneous slip and in an extensive plastic deformation within the heat treated base material (UAZ); ductile fracture ultimately occurred by internal necking which is typical of equiaxed near- α Ti-alloys [52].

Investigations corroborating a weakening in the vicinity of an as-welded Ti6242 LFW joint were reported by the authors in [28] during High-Cycle Fatigue (HCF) tests. These results showed that, despite failing in the base material under monotonic tensile test, the plastic activity initiated at 1.5 mm from the weld center line (i.e. in the oscillating HAZ). However the authors in [28] attributed this early plastic activity solely to the probable presence of residual stresses as reported in [15] in Ti64 LFW assemblies. Four among five of these HCF failures occurred in this early plasticized macro-zone; the crack was mostly composed of α grain facets. However, to the author's knowledge, no comparable fractographies of the as-welded Ti6242 LFW joint nor mechanical characterization of the weld after PWHT was found in the literature for

comparison purposes. The difference of approximately ten percent (-10%) in the stiffness and/or the yield stresses measured in the base material compared to the ones provided by the manufacturer could be imputed to a sample size effect.

4. Conclusion

The tensile responses of both Ti17 and Ti6242 LFW joints were investigated before and after a heat treatment, the following conclusions on the contributions of this post-weld heat treatment to the improvement of the local mechanical behaviors can be drawn:

1) The soft and mechanically unstable as-welded Ti17 joint was characterized by significantly heterogeneous properties both in the elastic and plastic domain mostly related to the dissolution of the hardening α precipitates in favor of an anisotropic $\beta_{\text{metastable}}$ phase. The latter was subjected to intense slip and different extent of stress-induced martensitic transformations in the joint core depending on the local microstructural features (i.e. grain size, dislocation density and chemical composition). This behavior resulted in worsened macroscopic mechanical properties compared to the ones of the as-received base material (i.e. stiffness, yield strength, and elongation at break). Heat treating the Ti17 joint permitted to recover an equilibrium $\alpha+\beta$ Widmanstätten microstructure across the whole assembly leading to both homogenized stiffness values and plastic behavior.

2) In the Ti6242, the extensive $\alpha\rightarrow\beta$ transformation during LFW in the joint core and the subsequent α' or α_s reprecipitation upon cooling resulted in a remarkable microstructure refinement and a consistent weld overmatch. An early plastic activity was detected at the vicinity of the refined joint due to the local dissolution of α_s platelets (initially hardening the β phase) in favor of a β_m matrix combined with a probable

resorption of the $(\text{Ti,Zr})_5\text{Si}_3$ and Ti_3Al particles. This changes led to a slight loss of stiffness in the joint core and to a major strain localization at the weakened vicinity of the latter. Subjecting the Ti6242 assembly to the heat treatment permitted to decompose the metastable phases into equilibrium $\alpha+\beta$ microstructures (homogenizing the stiffness) and to harden back the macro-zones initially softened by the process. A gradual microstructure refinement was preserved in the weld ensuring a remaining slight weld overmatch.

ACKNOWLEDGEMENT

The authors acknowledge the financial support from the French National Research Agency (ANR) through the OPTIMUM ANR-14-CE27-0017 project as well as the Spatial and Aeronautic Research Foundation, the Hauts-de-France Region and the European Regional Development Fund (ERDF) 2014/2020 for the funding of this work. The authors are also grateful to Dr A. El Bartali and A. Dos Santos for performing the micro-tensile tests at Centrale Lille as well as to ACB for providing LFW welded samples and Airbus for both their technical support.

DATA AVAILABILITY

The raw/processed data required to reproduce these findings can be shared on request.

References

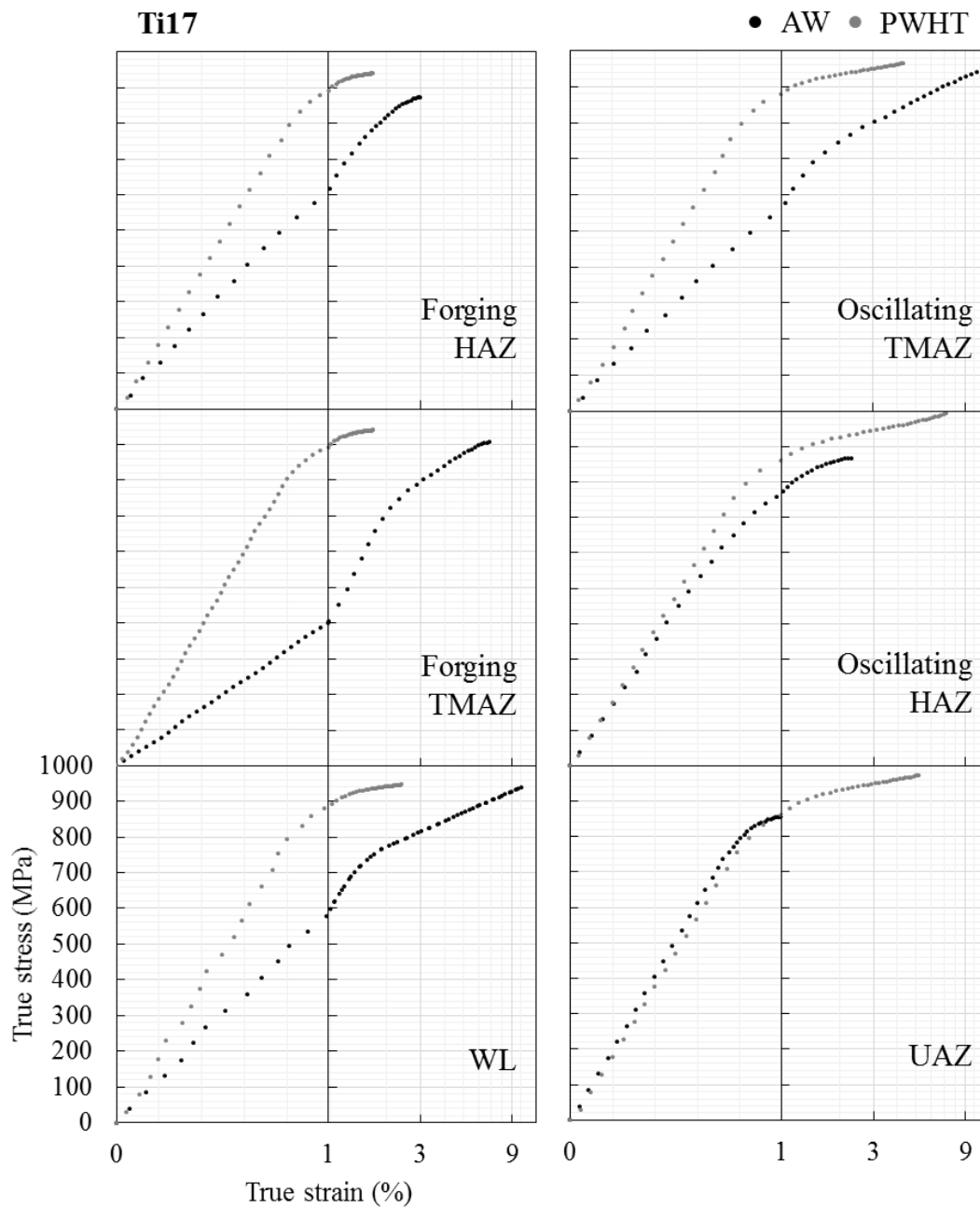
- [1] J. L. Huang, N. Warnken, J.-C. Gebelin, M. Strangwood, and R. C. Reed, "On the mechanism of porosity formation during welding of titanium alloys," *Acta Mater.*, vol. 60, no. 6–7, pp. 3215–3225, Apr. 2012.
- [2] M. J. Jr. Donachie, *Titanium A Technical Guide Second Edition*. 2000.
- [3] Z. Liu and G. Welsch, "Effects of oxygen and heat treatment on the mechanical properties of alpha and beta titanium alloys," *Metall. Trans. A*, vol. 19, no. 3, pp. 527–542, 1988.
- [4] T. Ando, K. Nakashima, T. Tsuchiyama, and S. Takaki, "Microstructure and mechanical properties of a high nitrogen titanium alloy," *Mater. Sci. Eng. A*, vol. 486, no. 1–2, pp. 228–234, Jul. 2008.
- [5] A. R. McAndrew, P. A. Colegrove, A. C. Addison, B. C. D. Flipo, M. J. Russell, and L. A. Lee, "Modelling of the workpiece geometry effects on Ti–6Al–4V linear friction welds," *Mater. Des.*, vol. 87, pp. 1087–1099, Dec. 2015.
- [6] A. R. McAndrew, P. A. Colegrove, C. Bühr, B. C. D. Flipo, and A. Vairis, "A literature review of Ti–6Al–4V linear friction welding," *Prog. Mater. Sci.*, vol. 92, pp. 225–257, Mar. 2018.
- [7] A. Vairis and M. Frost, "High frequency linear friction welding of a titanium alloy," *Wear*, vol. 217, pp. 117–131, 1998.
- [8] W. Li, A. Vairis, M. Preuss, and T. Ma, "Linear and rotary friction welding review," *Int. Mater. Rev.*, vol. 61, no. 2, pp. 71–100, Feb. 2016.
- [9] D. Ballat-Durand, S. Bouvier, M. Risbet, and W. Pantleon, "Multi-scale and multi-technic microstructure analysis of a linear friction weld of the metastable- β titanium alloy Ti–5Al–2Sn–2Zr–4Mo–4Cr (Ti17) towards a new Post-Weld Heat Treatment," *Mater. Charact.*, vol. 144, pp. 661–670, Oct. 2018.
- [10] D. Ballat-Durand, S. Bouvier, M. Risbet, and W. Pantleon, "Through analysis of the microstructure changes during linear friction welding of the near- α titanium alloy Ti–6Al–2Sn–4Zr–2Mo (Ti6242) towards microstructure optimization," *Mater. Charact.*, vol. 151, pp. 38–52, May 2019.
- [11] G. W. Stachowiak and A. W. Batchelor, *Engineering Tribology*. 2001.
- [12] G. Lütjering and J. C. Williams, *Titanium*. Berlin, Heidelberg: Springer Berlin Heidelberg, 2003.
- [13] I. Weiss and S. L. Semiatin, "Thermomechanical processing of beta titanium alloys—an overview," *Mater. Sci. Eng. A*, vol. 243, no. 1, pp. 46–65, 1998.
- [14] M. Karadge, M. Preuss, C. Lovell, P. J. Withers, and S. Bray, "Texture development in Ti–6Al–4V linear friction welds," *Mater. Sci. Eng. A*, vol. 459, no. 1–2, pp. 182–191, Jun. 2007.
- [15] J. Romero, M. M. Attallah, M. Preuss, M. Karadge, and S. E. Bray, "Effect of the forging pressure on the microstructure and residual stress development in Ti–6Al–4V linear friction welds," *Acta Mater.*, vol. 57, no. 18, pp. 5582–5592, Oct. 2009.
- [16] M. M. Attallah, M. Preuss, and S. Bray, "Microstructural development during linear friction welding of titanium alloys," *Trends Weld. Res. 2008*, pp. 486–491, 2009.
- [17] G. Buffa *et al.*, "Experimental and Numerical Analysis of Microstructure Evolution during Linear Friction Welding of Ti6Al4V," *Procedia Manuf.*, vol. 1, pp. 429–441, 2015.
- [18] J. C. Stinville, F. Bridier, D. Ponsen, P. Wanjara, and P. Bocher, "High and low cycle fatigue behavior of linear friction welded Ti–6Al–4V," *Int. J. Fatigue*, vol. 70, pp. 278–288, Jan. 2015.
- [19] Y. Ji, Z. Chai, D. Zhao, and S. Wu, "Linear friction welding of Ti–5Al–2Sn–2Zr–4Mo–4Cr alloy with dissimilar microstructure," *J. Mater. Process. Technol.*, vol. 214, no. 4, pp. 979–987, Apr. 2014.
- [20] W.-Y. Li, T. Ma, and S. Yang, "Microstructure Evolution and Mechanical Properties of Linear Friction Welded Ti–5Al–2Sn–2Zr–4Mo–4Cr (Ti17) Titanium Alloy Joints," *Adv. Eng. Mater.*, vol. 12, no. 1–2, pp. 35–43, Feb. 2010.
- [21] E. Dalgaard, P. Wanjara, J. Gholipour, X. Cao, and J. J. Jonas, "Linear friction welding of a near- β titanium alloy," *Acta Mater.*, vol. 60, no. 2, pp. 770–780, Jan. 2012.
- [22] W. A. Baeslack, "Characterization of Solid-Phase Welds Between Ti–6Al–2Sn–4Zr–2Mo–0.1Si and Ti–13.5Al–21.5Nb Titanium Aluminide," *Mater. Charact.*, vol. 33, pp. 357–367, 1994.
- [23] S. D. Meshram and T. Mohandas, "Influence of matrix microstructure on aging response of near alpha titanium alloy (IMI834) parent metal and welds on toughness," *Mater. Sci. Technol.*, vol. 27, no. 1, pp. 235–239, Jan. 2011.
- [24] E. Dalgaard, P. Wanjara, J. Gholipour, and J. J. Jonas, "Linear Friction Welding of a Forged Near- α Titanium Alloy," *Mater. Sci. Forum*, vol. 706–709, pp. 211–216, Jan. 2012.
- [25] P. Frankel, M. Preuss, A. Steuwer, P. J. Withers, and S. Bray, "Comparison of residual stresses in Ti–6Al–4V and Ti–6Al–2Sn–4Zr–2Mo linear friction welds," *Mater. Sci. Technol.*, vol. 25, no. 5, pp. 640–650, May 2009.

- [26] B. H. Tao, Q. Li, Y. H. Zhang, T. C. Zhang, and Y. Liu, "Effects of post-weld heat treatment on fracture toughness of linear friction welded joint for dissimilar titanium alloys," *Mater. Sci. Eng. A*, vol. 634, pp. 141–146, May 2015.
- [27] C. Zhang, T. Zhang, Y. Ji, and J. Huang, "Effects of heat treatment on microstructure and microhardness of linear friction welded dissimilar Ti alloys," *Trans. Nonferrous Met. Soc. China*, vol. 23, no. 12, pp. 3540–3544, Dec. 2013.
- [28] J. M. Garcia and T. F. Morgeneuer, "Strength and fatigue strength of a similar Ti-6Al-2Sn-4Zr-2Mo-0.1Si linear friction welded joint," *Fatigue & Fracture of Engineering Materials & Structures*, 2019.
- [29] J. M. Garcia, F. Gaslain, V. ESIN, and T. F. Morgeneuer, "Effect of a thermal treatment on the tensile and fatigue properties of similar Ti17 Linear Friction Welding joints and Ti17 parent material," *Mater. Charact.*
- [30] ASM International, Ed., *Metallography and microstructures*, New ed. Metals Park, Ohio: American Society for Metals, 2004.
- [31] D. Mainprice, R. Hielscher, and H. Schaeben, "Calculating anisotropic physical properties from texture data using the MTEX open-source package," *Geol. Soc. Lond. Spec. Publ.*, vol. 360, no. 1, pp. 175–192, 2011.
- [32] C. Eberl, *Digital Image Correlation and Tracking*. 2010.
- [33] G. Besnard, S. Guérard, S. Roux, and F. Hild, "A space–time approach in digital image correlation: Movie-DIC," *Opt. Lasers Eng.*, vol. 49, no. 1, pp. 71–81, Jan. 2011.
- [34] E. Aeby-Gautier, B. Denand, J. Teixeira, M. Dehmas, B. Appolaire, and A. Settefrati, "Influence of microstructure on tensile properties of β -metastable Ti 17 alloy.," p. 5.
- [35] E. Aeby-Gautier *et al.*, "Isothermal α' formation in β metastable titanium alloys," *J. Alloys Compd.*, vol. 577, pp. S439–S443, Nov. 2013.
- [36] T. Grosdidier, Y. Combres, and E. Gautier, "Effect of Microstructure Variations on the Formation of Deformation-Induced Martensite and Associated Tensile Properties in a Beta-Metastable Ti-Alloy," *Metall. Mater. Trans. A*, p. 12, 2000.
- [37] Y. T. Lee, M. Peters, and G. Welsch, "Elastic moduli and tensile and physical properties of heat-treated and quenched powder metallurgical Ti-6Al-4V alloy," *Metall. Trans. A*, vol. 22, no. 3, pp. 709–714, Mar. 1991.
- [38] P. Castany, A. Ramarolahy, F. Prima, P. Laheurte, C. Curfs, and T. Gloriant, "In situ synchrotron X-ray diffraction study of the martensitic transformation in superelastic Ti-24Nb-0.5N and Ti-24Nb-0.5O alloys," *Acta Mater.*, vol. 88, pp. 102–111, Apr. 2015.
- [39] M. Niinomi, T. Akahori, and M. Nakai, "In situ X-ray analysis of mechanism of nonlinear super elastic behavior of Ti–Nb–Ta–Zr system beta-type titanium alloy for biomedical applications," *Mater. Sci. Eng. C*, vol. 28, no. 3, pp. 406–413, Apr. 2008.
- [40] E. Lee, R. Banerjee, S. Kar, D. Bhattacharyya, and H. L. Fraser, "Selection of α variants during microstructural evolution in α/β titanium alloys," *Philos. Mag.*, vol. 87, no. 24, pp. 3615–3627, Aug. 2007.
- [41] S. Fréour, E. Lacoste, M. François, and R. Guillén, "Determining Ti-17 β -Phase Single-Crystal Elasticity Constants through X-Ray Diffraction and Inverse Scale Transition Model," *Mater. Sci. Forum*, vol. 681, pp. 97–102, Mar. 2011.
- [42] J. Nejezchlebová *et al.*, "The effect of athermal and isothermal ω phase particles on elasticity of β -Ti single crystals," *Acta Mater.*, vol. 110, pp. 185–191, May 2016.
- [43] M. Tane, Y. Okuda, Y. Todaka, H. Ogi, and A. Nagakubo, "Elastic properties of single-crystalline ω phase in titanium," *Acta Mater.*, vol. 61, no. 20, pp. 7543–7554, Dec. 2013.
- [44] H. Ikehata, N. Nagasako, T. Furuta, A. Fukumoto, K. Miwa, and T. Saito, "First-principles calculations for development of low elastic modulus Ti alloys," *Phys. Rev. B*, vol. 70, no. 17, Nov. 2004.
- [45] T. W. Duerig, "Formation and reversion of stress induced martensite in Ti-10V-2Fe-3Al," *Acta Met.*, vol. 30, pp. 2161–2172, 1982.
- [46] T. Narutani, "Effect of deformation-induced martensitic transformation on the plastic behavior of metastable austenitic stainless steel," *Mater. Trans.*, vol. 30, no. 1, 1989.
- [47] W. Elmay, S. Berveiller, E. Patoor, T. Gloriant, F. Prima, and P. Laheurte, "Texture evolution of orthorhombic α' titanium alloy investigated by in situ X-ray diffraction," *Mater. Sci. Eng. A*, vol. 679, pp. 504–510, Jan. 2017.
- [48] A. Paradkar, S. V. Kamat, A. K. Gogia, and B. P. Kashyap, "Effect of Al and Nb on the trigger stress for stress-induced martensitic transformation during tensile loading in Ti–Al–Nb alloys," *Mater. Sci. Eng. A*, vol. 487, no. 1–2, pp. 14–19, Jul. 2008.
- [49] M. Tokizane, "The effect of tensile pre-straining on nucleation of martensite in an Fe-Ni-C alloy," *Scr. Metall.*, vol. 10, 1976.

- [50] K. Smidoda, W. Gottschalk, and H. Gleiter, "Diffusion in migrating interfaces," *Acta Metall.*, vol. 26, no. 12, pp. 1833–1836, Dec. 1978.
- [51] A. Gysler, G. Lütjering, and V. Gerold, "Deformation behavior of age-hardened Ti-Mo alloys," *Acta Metall.*, vol. 22, 1974.
- [52] V. A. Joshi, *Titanium alloys: an atlas of structures and fracture features*. Boca Raton, Fla.: Taylor & Francis, 2006.
- [53] R. Liang, Y. Ji, S. Wang, and S. Liu, "Effect of Microstructure on Fracture Toughness and Fatigue Crack Growth Behavior of Ti17 Alloy," *Metals*, vol. 6, no. 8, p. 186, Aug. 2016.
- [54] X. Shi, W. Zeng, and Q. Zhao, "The effects of lamellar features on the fracture toughness of Ti-17 titanium alloy," *Mater. Sci. Eng. A*, vol. 636, pp. 543–550, Jun. 2015.
- [55] Y. T. Lee and G. Welsch, "Young's Modulus and Damping of Ti-6Al-4V Alloy as a Function of Heat Treatment and Oxygen Concentration," *Mater. Sci. Eng. A*, vol. 128, pp. 77–89, 1990.
- [56] W. Mei, J. Sun, and Y. Wen, "Martensitic transformation from β to α' and α'' phases in Ti-V alloys: A first-principles study," *J. Mater. Res.*, vol. 32, no. 16, pp. 3183–3190, Aug. 2017.
- [57] D. Banerjee and J. C. Williams, "Microstructure and Slip Character in Titanium Alloys," *Def. Sci. J.*, vol. 36, no. 2, pp. 191–206, Jan. 1986.
- [58] S. Malinov, W. Sha, Z. Guo, C. C. Tang, and A. E. Long, "Synchrotron X-ray diffraction study of the phase transformations in titanium alloys," *Mater. Charact.*, vol. 48, no. 4, pp. 279–295, Jun. 2002.

APPENDIX A

True stress/strain curves (truncated at the onset of macroscopic necking) in the joint macro-zones of the Ti17 LFW assemblies before and after the PWHT; the vertical and horizontal axis represent the true stress and true strain respectively; the graph scales and units are provided at the left-bottom plot; macroscopic necking occurred at 3.1% and 4.22% of macroscopic engineering strain for the AW and PWHT respectively.



APPENDIX B

True stress/strain curves (truncated at the onset of macroscopic necking) in the joint macro-zones of the Ti6242 LFW assemblies before and after the PWHT; the vertical and horizontal axis represent the true stress and true strain respectively; the graph scales and units are provided at the left-bottom plot; macroscopic necking occurred at 2.78% and 7.92% of macroscopic engineering strain for the AW and PWHT respectively.

